


Exploring Adaptive Phenotypes for the Human Calcium-Sensing Receptor Polymorphism R990G

Barbara Sinigaglia,¹ Jorge Escudero,¹ Simone A. Biagini,¹ Jorge Garcia-Calleja,¹ Josep Moreno,² Begoña Dobon,¹ Sandra Acosta,^{1,3} Mayukh Mondal,^{4,5} Sandra Walsh,¹ Gabriela Aguilera,¹ Mònica Vallès,¹ Stephen Forrow,⁶ Juan Martin-Caballero,² Andrea Bamberg Migliano,⁷ Jaume Bertranpetit,¹ Francisco J Muñoz,⁸ and Elena Bosch ^{1,*}

¹Institut de Biologia Evolutiva (UPF-CSIC), Departament de Medicina i Ciències de la Vida, Universitat Pompeu Fabra, Parc de Recerca Biomèdica de Barcelona, Barcelona 08003, Spain

²PCB-PRBB Animal Facility Alliance, Parc de Recerca Biomèdica de Barcelona, Barcelona 08003, Spain

³UB Institute of Neuroscience, Department of Pathology and Experimental Therapeutics, Universitat de Barcelona, Barcelona 08007, Spain

⁴Institute of Genomics, University of Tartu, Tartu 51010, Estonia

⁵Institute of Clinical Molecular Biology, Christian-Albrechts-Universität zu Kiel, Kiel 24118, Germany

⁶Mouse Mutant Core Facility, Institute for Research in Biomedicine (IRB), Barcelona 08028, Spain

⁷Human Evolutionary Ecology Group, Department of Evolutionary Anthropology, University of Zurich, Zurich 8057, Switzerland

⁸Laboratory of Molecular Physiology, Departament de Medicina i Ciències de la Vida, Universitat Pompeu Fabra, Parc de Recerca Biomèdica de Barcelona, Barcelona 08003, Spain

*Corresponding author: E-mail: elena.bosch@upf.edu.

Associate editor: Brandon Gaut

Abstract

Rainforest hunter–gatherers from Southeast Asia are characterized by specific morphological features including a particularly dark skin color (D), short stature (S), woolly hair (W), and the presence of steatopygia (S)—fat accumulation localized in the hips (DSWS phenotype). Based on previous evidence in the Andamanese population, we first characterized signatures of adaptive natural selection around the calcium-sensing receptor gene in Southeast Asian rainforest groups presenting the DSWS phenotype and identified the R990G substitution (rs1042636) as a putative adaptive variant for experimental follow-up. Although the calcium-sensing receptor has a critical role in calcium homeostasis by directly regulating the parathyroid hormone secretion, it is expressed in different tissues and has been described to be involved in many biological functions. Previous works have also characterized the R990G substitution as an activating polymorphism of the calcium-sensing receptor associated with hypocalcemia. Therefore, we generated a knock-in mouse for this substitution and investigated organismal phenotypes that could have become adaptive in rainforest hunter–gatherers from Southeast Asia. Interestingly, we found that mouse homozygous for the derived allele show not only lower serum calcium concentration but also greater body weight and fat accumulation, probably because of enhanced preadipocyte differentiation and lipolysis impairment resulting from the calcium-sensing receptor activation mediated by R990G. We speculate that such differential features in humans could have facilitated the survival of hunter–gatherer groups during periods of nutritional stress in the challenging conditions of the Southeast Asian tropical rainforests.

Key words: genetic adaptation, CaSR, SE Asian populations, pygmy phenotype.

Introduction

The Andamanese are the Indigenous people from the Andaman Islands, situated in the north-eastern Indian Ocean, where they have lived in genetic isolation following a hunter–gatherer lifestyle till nearly present times. Since the early colonial period, they underwent a rapid population decline and nowadays some Andamanese groups are

also experiencing a cultural shift toward a more sedentary lifestyle (Venkateswar 2004). Like other hunter–gatherers living in the tropical rainforests of Africa, Asia, and Australia, the Andamanese present characteristic phenotypic features including dark skin (D), very short stature (S), woolly hair (W), and sporadic steatopygia (S) (i.e. enhanced development and accumulation of fat on the

Received: January 18, 2024. Revised: January 23, 2024. Accepted: January 23, 2024

© The Author(s) 2024. Published by Oxford University Press on behalf of Society for Molecular Biology and Evolution.

This is an Open Access article distributed under the terms of the Creative Commons Attribution-NonCommercial License (<https://creativecommons.org/licenses/by-nc/4.0/>), which permits non-commercial re-use, distribution, and reproduction in any medium, provided the original work is properly cited. For commercial re-use, please contact journals.permissions@oup.com

Open Access

buttocks). Hereafter, this complete set of characters will be referred to as the DSWS phenotype. A common origin but also convergent adaptations to the environmental challenges found in their corresponding rainforest habitats and/or resulting from their lifestyle have been postulated to explain the shared DSWS phenotype across different hunter–gatherer groups (Perry and Dominy 2009; Verdu et al. 2009). Previously, the analysis of whole-genome sequences from 10 Onge (ONG) and Jarawa (JAR) individuals from the Andaman Islands and 60 mainland Indian individuals detected signatures of strong positive selection on genes related to human body size and recapitulated the Andamanese short stature when using a polygenic score based on height-associated variants (Mondal et al. 2016). Among the top 20 most differentiated nonsynonymous and stop–gain single-nucleotide polymorphisms (SNPs) between Andamanese and mainland India found on candidate genes for positive selection in the former group, we identified the R990G substitution (rs1042636) at the calcium (Ca)-sensing receptor gene (CASR), with a Combined Annotation Dependent Depletion (CADD) score value of 18.42, as a putative adaptive variant for experimental follow-up.

The Ca-sensing receptor (CaSR) plays a critical role in Ca homeostasis by directly regulating urinary Ca excretion and parathyroid hormone (PTH) secretion, while through its receptor (PTH1R) and the stimulation of 1,25-dihydroxy vitamin D, it acts on the bone, kidney, and intestine to restore the appropriate circulating Ca levels in the body (Ho et al. 1995; Thakker et al. 2016). Moreover, CaSR also participates in modulating bone formation and resorption, as well as in the development of the bone growth plate (Chang et al. 2008; Riccardi et al. 2013; Wang et al. 2013; Goltzman and Hendy 2015). In particular, whereas early chondrocyte differentiation in the cartilaginous growth plate is activated via the PTH-related peptide (PTHrP)/PTH1R signaling, the insulin-like growth factor 1 (IGF1)/IGF1 receptor (IGF1R) and the Ca^{2+} /CaSR signaling pathways mediate the terminal maturation of the hypertrophic chondrocytes as well as their subsequent transformation into the osteoblastic lineage (Wang et al. 2013; Santa Maria et al. 2016). However, the CASR gene is expressed across a wide range of tissues and has been involved in many other diverse biological functions including epidermal development, keratinocyte differentiation, hair follicle morphogenesis (Turksen and Troy 2003; Elsholz et al. 2014), human taste perception (Ohsu et al. 2010), as well as in preadipocyte proliferation and differentiation (Villaruel et al. 2013). Previous in vitro studies have shown that the derived allele of the R990G substitution results in a gain-of-function of CaSR, which renders the receptor more sensitive to Ca^{2+} (Vezzoli et al. 2007; Ranieri et al. 2013). As expected for a CaSR activating variant, the 990G allele is associated with increased susceptibility to primary hypercalciuria (Vezzoli et al. 2007), decreased serum Ca (Scillitani et al. 2004; Kapur et al. 2010), and an increased risk of kidney stone disease (Guha et al. 2015). However, the pleiotropic nature of the CASR gene complicates any direct inference of a putative adaptive

phenotype for such activating substitution in the Andamanese.

Several general (Ho et al. 1995; Hough et al. 2004; Dong et al. 2015; Hannan et al. 2015) and tissue-specific (Chang et al. 2008; Chang et al. 2010; Toka et al. 2012) knock-out (KO) mice and knock-in (KI) mice for different inactivating and activating CaSR mutations have been obtained for the CASR gene and allowed not only to infer many details of the CaSR function but also to successfully recapitulate the disease phenotype of human illnesses such as familial hypocalciuria hypercalcemia, severe neonatal hyperthyroidisms, and autosomal dominant hypocalcemia. In turn, KI mouse models have proven to be a good strategy to experimentally validate the associated phenotype of adaptive alleles in the human *FOXP2* (Enard et al. 2009; Schreiweis et al. 2014) and *EDAR* (Kamberov et al. 2013) genes. Thus, the generation of a KI mouse for the R990G human substitution should be a promising approach to pinpoint any differential (and putative adaptive) phenotype across all those pleiotropic functions of CaSR potentially shared between humans and mice.

In this work, we first compiled whole-genome sequencing data generated in the Andamanese and other SE Asian hunter–gatherer groups presenting the DSWS phenotype and investigated the CASR region for signatures of recent positive selection by specifically interrogating the site frequency spectrum and the patterns of linkage disequilibrium and population differentiation. Next, we generated a KI mouse for the human R990G substitution using the clustered regularly interspaced short palindromic repeats (CRISPR)-Cas9 editing technology and assessed its phenotypic impact by exploring for potential differences between the homozygous carriers of the ancestral (R990) and the derived (990G) allele, respectively.

Results

Signals of Positive Selection and the R990G Substitution

The CASR gene was identified by Mondal et al. (2016) as a strong candidate for positive selection in the Andamanese when applying a hierarchical boosting framework that combined 8 neutrality tests to uncover the patterns of variation expected under a hard sweep scenario while controlling for population demography (Mondal et al. 2016). Here, we computed 4 individual tests of positive selection using the same whole-genome sequencing data in the Andamanese and present them along 200 kb upstream and downstream the ~ 108 kb CASR gene region (supplementary data set S1, Supplementary Material online). In particular, we calculated Tajima's D (Tajima 1989), Fay and Wu's H (Fay and Wu 2000), and XP-EHH (Sabeti et al. 2007) comparing Andamanese versus Yoruba, which were included in the boosting framework of Mondal et al. (2016), as well as XP-EHH comparing Andamanese versus Irula, a Dravidian-speaking tribal population from S India. In agreement with previous results

(Mondal et al. 2016), departures from genome-wide empirical values were found in the *CASR* gene in each of the 4 selection tests (Fig. 1A and B). While significantly negative values of Tajima's *D* and Fay and Wu's *H* indicate an excess of low-frequency polymorphisms and high-frequency derived SNPs relative to genome-wide expectations, respectively, the XP-EHH statistic points to unusually extended haplotype homozygosity in the Andamanese when compared with either the Yoruba or the Irula populations. After functionally annotating all variants in the *CASR* gene region and comparing their allele frequencies between the JAR and ONG Andamanese and 6 mainland Indian populations, we retained 165 SNPs with allele frequency differences >25%. Among these, 10 variants presented a CADD score > 10 (i.e. are predicted within the 10% most deleterious variants of the human genome) including the R990G substitution (rs1042636), which was found to have the third highest absolute allele frequency difference (i.e. 87.5% in JAR and ONG Andamanese and 22% in mainland India; see [supplementary data set S2, Supplementary Material](#) online). However, while rs1042636 presented the highest CADD score value (18.42), the top 2 putative functionally differentiated SNPs (rs13059382 and rs7644981) were intronic and presented CADD score values <15 (i.e. the median value for all possible canonical splice site changes and nonsynonymous variants in CADD v1.0 and accepted cutoff to identify pathogenic variants; Kircher et al. 2014). Thus, the R990G substitution was confirmed to be the most probable putative candidate variant.

By exploring the worldwide frequencies of the derived 990G allele in populations from the 1,000 G Project Phase 3 (Auton et al. 2015) and in an extended data set of 12 additional populations from SE Asia (see [Materials and Methods](#)), we detected the highest frequencies in several hunter-gatherer groups presenting the DSWS phenotype (100% in JAR, 97% in Aeta, 85% in Agta, 83% in Kintaq, 78% in Jehai, and 75% in ONG and Mamanwa) while finding intermediate values in East Asia (52%) but much lower presence in other populations from Mid-South Asia (26%), Europe (7%), and Africa (3%; see Fig. 1C). In contrast, the frequency of the 990G allele in populations from Papua New Guinea was clearly lower than that in the East Asian hunter-gatherer groups with the DSWS phenotype (ranging from 40% in Kosipe to 0% in Sepik). Furthermore, in accordance with the observed allele frequencies, when grouping these populations into 3 main SE Asian groups, we detected signatures of positive selection along the *CASR* region with XP-EHH and SF select in Malaysia and the Philippines but not in Papua New Guinea (Fig. 1B, [supplementary fig. S1](#) and [data set S1, Supplementary Material](#) online). Similarly, departures from neutrality were only observed in the Aeta and Agta from the Philippines and in the Kintaq from Malaysia when analyzing each individual Malaysian and Philippine population versus the Koinambe with the XP-EHH statistic ([supplementary fig. S2](#) and [data set S3, Supplementary Material](#) online). Consequently, the R990G substitution can be hypothesized

to be a putative adaptive variant targeted by positive selection in several hunter-gatherer groups displaying the DSWS phenotype in SE Asia besides the Andamanese, although it is still not possible to entirely rule out complex demographic causes for these patterns. Nonetheless, the 990G variant was found consistently on the same core haplotype background (when analyzing ~87.63 kb centered on rs1042636) in all geographical regions where the polymorphism segregates ([supplementary data set S4, Supplementary Material](#) online), and no signals of selection were found when inspecting the East and South Asian populations available at the 1,000 Genomes Selection Browser 1.0 (Pybus et al. 2014) (<https://hsb.upf.edu/>) and the PopHumanScan browser (Casillas et al. 2018) (<https://pophuman.uab.cat/>) (see details in [supplementary note S1, Supplementary Material](#) online). Therefore, the R990G substitution probably has a single origin and appears to be associated with unusually high-frequency extended haplotypes and with neutral deviations in the site frequency spectrum only in hunter-gatherer groups from SE Asia. We next investigated the local genealogical tree of the candidate SNP rs1042636 (chr3:122003769, GRCh37/hg19) with Relate (Speidel et al. 2019) and estimated its selection coefficient and past allele frequency trajectory with CLUES (Stern et al. 2019). When analyzing all 3 hunter-gatherer groups from SE Asia together, we found moderate evidence ($\log_{RT} = 5.289$) for weak selection ($s = 0.0025$) acting within the last 1,000 generations before present (i.e. 28,000 yrs ago assuming 28 yrs per generation; [supplementary figs. S3 to S4, Supplementary Material](#) online). However, when analyzing each group separately, we were able to confirm a likely scenario for moderate selection only in the Andamanese ($s = 0.0044$; $\log_{RT} = 2.707$; [supplementary table S1](#) and [fig. S5, Supplementary Material](#) online).

Generation and Maintenance of a KI Mouse Model

Since the ancestral Arg allele (R990) is present in wild-type mice, we edited via CRISPR-Cas9 the corresponding orthologous nucleotide position of the mouse *Casr* gene to generate the R990G substitution in the encoded protein ([supplementary fig. S6, Supplementary Material](#) online). From the obtained mosaics, we generated 2 independent R990G KI mouse lines, henceforth denoted as lines 7 and 15, and explored for potential differences between the ancestral (R990) and derived (990G) homozygous sibling carriers resulting from several heterozygous crosses within each line (see details in [supplementary fig. S7, Supplementary Material](#) online). All potential off-targets predicted by the Benchling gRNA designing tool and the correct editing of *Casr* were checked by Sanger sequencing in the F1 heterozygous founders or corresponding F2 descendants. All animals had free access to water and were fed ad libitum on a standard diet (unless otherwise indicated) under the same environmental conditions. Both R990 and 990G homozygote littermates were born at expected Mendelian ratios, appeared healthy and had normal longevity.

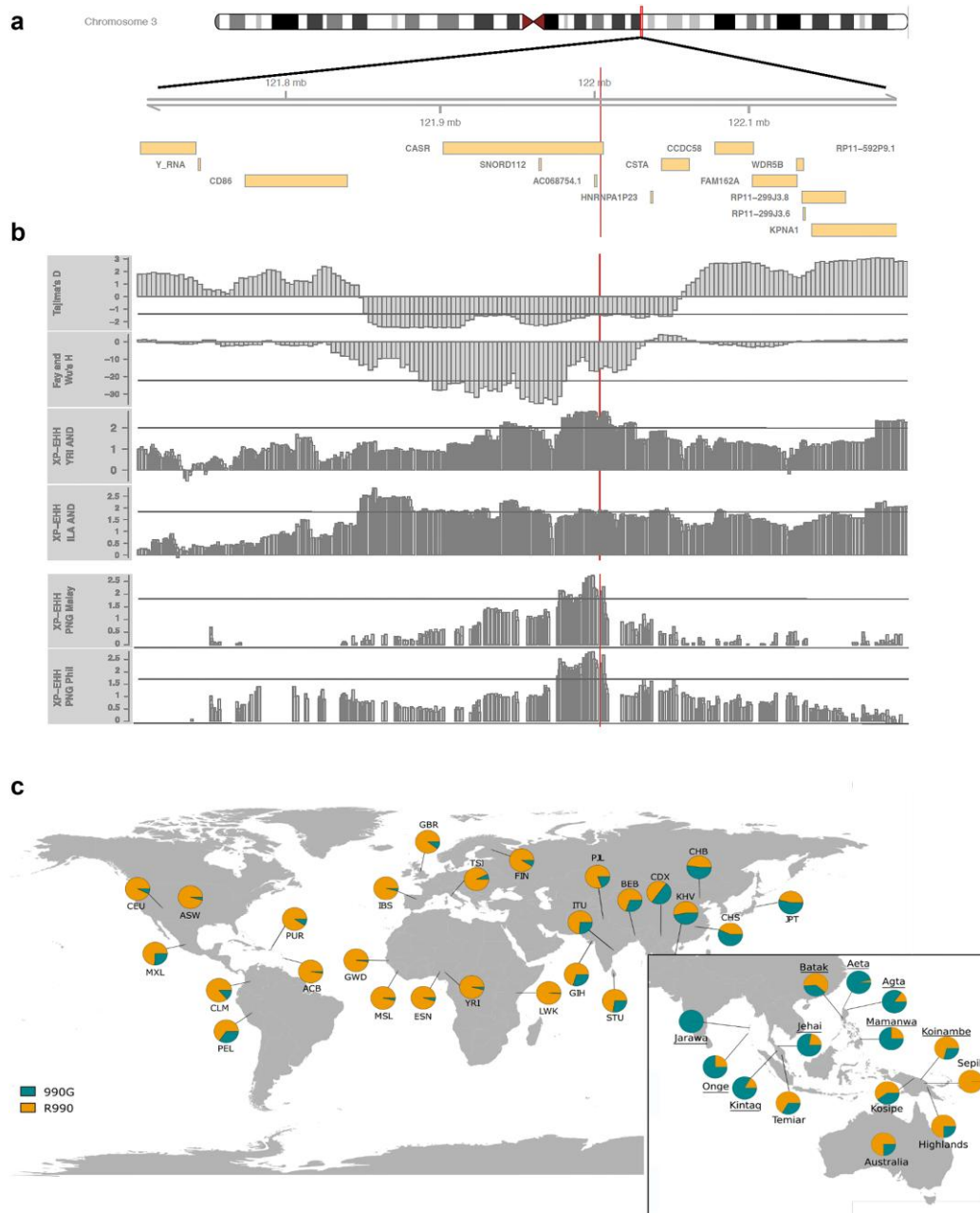


Fig. 1. Signals of positive selection in the CASR gene region and worldwide frequencies for the R990G substitution. a) On the top, the location of the CASR gene region on chromosome 3. Below, zoom-in with Ensembl gene tracks comprising 200 kb upstream and downstream of the CASR gene. b) Tests of positive selection in the Andamanese (Tajima's D, Fay, and Wu's H, XP-EHH comparing Andamanese vs. Yoruba, and XP-EHH comparing Andamanese vs. Irula, a Dravidian-speaking tribal population from S India) as well as in Malaysian and Philippine hunter-gather groups presenting the DSWS phenotype (XP-EHH comparing each SE Asian population group vs. Papua New Guinea). For each population and selection statistic, the horizontal bar indicates the top or bottom 2.5th percentile of their respective genome-wide distribution (z-scores are available in [supplementary data set S1, Supplementary Material](#) online). The position of the CaSR R990G polymorphism is represented by the vertical line across the panels. c) Worldwide allele frequencies of the CaSR R990G polymorphism. Each pie graph represents the allele frequency in 1 population. Population names from the 1,000 G Project Phase 3 are abbreviated as follows: CHB, Han Chinese in Beijing; JPT, Japanese in Tokyo; CHS, Southern Han Chinese; CDX, Chinese Dai in Xishuangbanna; KHV, Kinh in Ho Chi Minh City; CEU, Utah Residents (CEPH) with Northern and Western European Ancestry; TSI, Toscani in Italia; FIN, Finnish in Finland; GBR, British in England and Scotland; IBS, Iberian Population in Spain; YRI, Yoruba in Ibadan, Nigeria; LWK, Luhya in Webuye, Kenya; GWD, Gambian in Western Divisions in the Gambia; MSL, Mende in Sierra Leone; ESN, Esan in Nigeria; ASW, Americans of African Ancestry in SW USA; ACB, African Caribbeans in Barbados; MXL, Mexican Ancestry from Los Angeles, USA; PUR, Puerto Ricans from Puerto Rico; CLM, Colombians from Medellin, Colombia; PEL, Peruvians from Lima, Peru; GIH, Gujarati Indian from Houston, Texas; PJI, Punjabi from Lahore, Pakistan; BEB, Bengali from Bangladesh; STU, Sri Lankan Tamil from the UK; and ITU, Indian Telugu from the UK. Populations from SE Asia shown in the square are hunter-gatherers, and underlined populations display the DSWS phenotype.

Differences in Weight Growth Curves and Body Composition

Given the previously recognized role of CaSR in modulating serum mineral disturbances (Scillitani et al. 2004; Vezzoli et al. 2007; Kapur et al. 2010; Kanai et al. 2018), as well as in promoting preadipocyte proliferation (Rocha et al. 2015; Bravo-Sagua et al. 2016) and regulating adipocyte lipolysis and adipogenesis (He et al. 2012; Villarroel et al. 2013), we first investigated whether the R990G polymorphism could be associated with differences in weight growth and body composition, as these could in turn be related to the DSWS phenotype. Weekly body weight changes were recorded from wks 3 to 20 and compared between sexes (using 43 males and 43 females), lines (including a total of 46 and 40 animals for lines 7 and 15, respectively), and genotypes (with a total of 42 homozygotes R990 and 44 homozygotes 990G) using factorial analysis of variance (ANOVAs), as well as by using a mixed-model ANOVA with repeated measures across wks 4 to 12 (see [supplementary data set S5, Supplementary Material online](#)). When considering all mice together ($N = 86$), sex was the variable that most influenced body weight, explaining 46.35% of the total variation (average percentage across wks 4 to 12), whereas genotype and line also displayed weekly significant differences in body weight and explained 8.17% and 4.23% of the variation, respectively (see weekly details in [supplementary data set S5, Supplementary Material online](#)). Notably, homozygous carriers for the 990G allele displayed significantly higher body weight than homozygotes for the R990 allele in the whole set of animals ($N = 86$ with 42 R990 homozygotes and 44 990G homozygotes, repeated measures ANOVA, $P = 0.00003$) as well as when separating mice into the 2 generated lines ($N = 46$ with 22 R990 homozygotes and 24 990G homozygotes, repeated measures ANOVA, $P = 0.00028$ for line 7 and $P = 0.031$ for line 15 using $N = 40$ with 20 R990 homozygotes and 20 990G homozygotes; see weekly details in [supplementary data set S5, Supplementary Material online](#)). However, whereas the percentage of the body weight variation explained by the genotype was 13.46% in line 7 (average percentage across wks 4 to 12), in line 15, it explained only 4.74% of the variation. Accordingly, when separating mice by sex and line, an ANOVA with repeated measures across wks 4 to 12 showed significant differences in body weight between genotypes in both males ($N = 23$ with 11 R990 homozygotes and 12 990G homozygotes, $P = 0.022$) and females ($N = 23$ with 11 R990 homozygotes and 12 990G homozygotes, $P = 0.005$) in line 7 but only in males ($N = 20$ with 10 R990 homozygotes and 10 990G homozygotes, $P = 0.023$) in line 15 (Fig. 2A; [supplementary fig. S8 and data set S5, Supplementary Material online](#)). Notably, body weight differences between genotypes were replicated in a second cohort of animals including 42 mice from line 15 and 45 mice from line 7 (see [supplementary data set S5, Supplementary Material online](#)) that were subjected to a vitamin D-deficient diet from the 3rd to the 14th wk of age ($N = 87$ with 42 R990

homozygotes and 45 990G homozygotes, repeated measures ANOVA, $P = 0.032$). However, the percentage of body weight variation explained by genotype under vitamin D deficiency was lower than that observed under normal diet (2.98% vs. 8.17%, average percentage across wks 4 to 12). Moreover, under normal diet, homozygous carriers for the 990G allele were found to present higher body mass index (BMI) when analyzing all animals together ($N = 128$ including 65 R990 homozygotes and 63 990G homozygotes, Kruskal–Wallis test, $P = 0.035$) and when separating mice by sex ($N = 62$ females with 29 R990 homozygotes and 33 990G homozygotes, Mann–Whitney U Test, $P = 0.047$; $N = 66$ males with 36 R990 homozygotes and 30 990G homozygotes, Mann–Whitney U Test, $P = 0.035$) but only in the female group of line 7 when separating mice by line and sex ($N = 42$ including 18 R990 homozygotes and 24 990G homozygotes, Mann–Whitney U Test, $P = 0.021$) (Fig. 2B and [supplementary fig. S9, Supplementary Material online](#)). Since no statistically significant trend was observed between genotypes regarding the mice crown rump length ([supplementary data set S5, Supplementary Material online](#)), the observed differences on BMI can be mostly attributed to weight.

Finally, whole body fat and lean composition for 33 animals from line 7 under normal diet was determined with an EchoMRI instrument at 14 wks of age ([supplementary data set S6, Supplementary Material online](#)). Males and females significantly differed in their overall fat and lean content (Kruskal–Wallis test comparing 18 females and 15 males, $P = 0.021$ and $P < 0.001$, respectively) according to the higher weight of males when compared with females (Kruskal–Wallis test, $P < 0.001$; [supplementary fig. S10, Supplementary Material online](#)). Furthermore, although no differential pattern was detected when comparing body composition between genotypes and analyzing males and females together ($N = 33$ with 17 R990 homozygotes and 16 990G homozygotes) or only males ($N = 15$ including 8 R990 homozygotes and 7 990G homozygotes; [supplementary fig. S10 and data set S6, Supplementary Material online](#)), homozygous female carriers of the 990G allele presented significantly lower lean percentage ($N = 18$, Mann–Whitney U test comparing 9 R990 homozygotes to 9 990G homozygotes, $P = 0.031$), and marginally not significant higher overall fat ($N = 18$, Mann–Whitney U test, $P = 0.050$) than the homozygous female carriers of the R990 allele (Fig. 2C to E, [supplementary fig. S10 and data set S6, Supplementary Material online](#)).

No Differential Skeletal or Epidermal Phenotype

Since mutants of the *Casr* gene in mice have been associated with differential skeletal phenotypes (Chang et al. 2008; Riccardi et al. 2013; Wang et al. 2013; Goltzman and Hendy 2015), tibial cortical bone and trabecular bone at the proximal tibial metaphysis were analyzed *ex vivo* by micro-computed tomography on 28 animals under normal diet (including between 2 and 4 animals per sex, line, and genotype). However, no differences in bone micro-architecture were identified between the CaSR

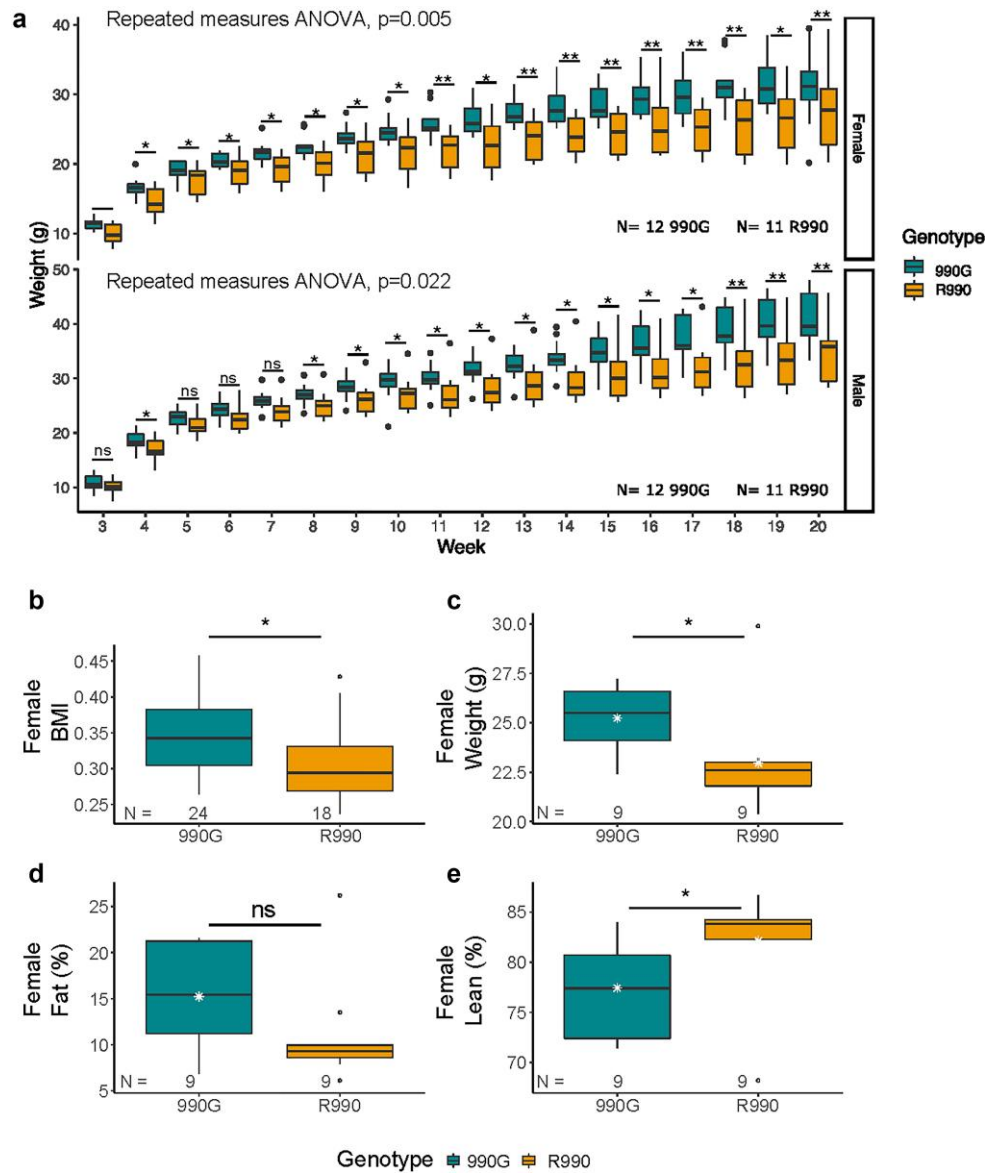


Fig. 2. Body weight growth curves, BMI, and body composition for CaSR R990G KI mice (line 7). a) Boxplots showing the differences in mice body weight from 3 to 20 wks of age between the homozygote carriers of the R990 (ancestral) and 990G (derived) alleles of the CaSR R990G polymorphism. * $P < 0.05$; ** $P < 0.005$; ns, not significance (1-way ANOVA). b) BMI at the final point (20 to 26 wks of age; females). c) Weight differences between genotypes on wk 14 of age for females analyzed with EchoMRI. d) Differences in female body fat percentage between genotypes as determined by EchoMRI analysis on wk 14 of age. e) Differences in female body lean percentage between genotypes as determined by EchoMRI analysis on wk 14 of age. * $P < 0.05$; ns, not significance (Mann-Whitney U test). For all boxplots, the line in the middle of each box represents the median for each group examined, and the edges of the box represent the first and third quartiles. Filled circles represent outliers (values > 1.5 and < 3 interquartile ranges from the edge of the box). Detailed significance levels for all tests are available in [supplementary data sets S5 and S6, Supplementary Material](#) online.

R990G genotypes ([supplementary data set S7](#) and [fig. S11, Supplementary Material](#) online). Similarly, since CaSR has been involved in epidermal differentiation ([Turksen and Troy 2003](#)), we also monitored wound healing and epidermis histology after performing 5 mm skin biopsy punches at 10 and 20 wks of age, but no major differences in epidermal thickness nor significant wound healing rate differences or differential reepithelization patterns were detected between the genotypes of the CaSR R990G substitution ([supplementary data set S8](#) and [fig. S12, Supplementary Material](#) online).

Differential Ca and Cholesterol Blood Biochemistries
 Since CaSR activation has been associated with altered Ca concentrations in blood and urine ([Scillitani et al. 2004](#); [Vezzoli et al. 2007](#); [Kapur et al. 2010](#)), we checked whether these could be detected in our mouse model. Similarly, given the known regulatory role of CaSR in the adipose tissue ([Bravo-Sagua et al. 2016](#)), we also investigated whether the R990G polymorphism could be associated with any differential lipidic pattern in blood that could facilitate the DSWs phenotype. Accordingly, blood and urine samples were taken between the 12 and 14 wks of age to analyze

16 different metabolites and hormones mostly related to Ca homeostasis and lipid metabolism (animals under normal diet; [supplementary data set S9, Supplementary Material](#) online). In agreement with the CaSR activation produced by the R990G substitution ([Vezzoli et al. 2007](#); [Ranieri et al. 2013](#)), male homozygous carriers for the 990G allele presented not only lower serum Ca ($N = 63$ males from both lines including 32 R990 homozygotes and 31 990G homozygotes, factorial ANOVA; $P = 0.017$) but also higher serum phosphorus ($N = 63$ males both lines, factorial ANOVA; $P = 0.004$; [Table 1](#)). No clear differential patterns between genotypes were found for urinary Ca and phosphorus excretion or the PTH and osteocalcin serum concentrations when testing a minimum of 5 animals per sex, genotype, and line ([supplementary data set S9, Supplementary Material](#) online). However, we found consistent significant differences in the high-density lipoprotein (HDL) and low-density lipoprotein (LDL) cholesterol levels between the CaSR R990G genotypes ([Table 1](#)) with the homozygous carriers for the 990G allele presenting significantly lower HDL and LDL blood concentrations when analyzing all animals ($N = 120$ including 56 R990 homozygotes and 64 990G homozygotes from both lines, factorial ANOVA; $P = 0.020$ and $P = 0.001$ for HDL and LDL differences between genotypes, respectively), only females ($N = 57$ including 24 R990 homozygotes and 33 990G homozygotes from both lines, factorial ANOVA; $P = 0.003$ and $P = 0.018$ for HDL and LDL, respectively), and line 15 animals ($N = 51$ including 26 R990 homozygotes and 25 990G homozygotes from both sexes, factorial ANOVA; $P = 0.016$ and $P = 0.002$ for HDL and LDL, respectively; as well as separating by sex, see details in [Table 1](#)).

Differential Phenotypes in the Liver and Fat

The higher body weight and lipidic changes observed in peripheral blood associated with the 990G variant led us to investigate whether further distinctive metabolic features could be distinguished in the liver and adipose tissue. Liver biopsies from 92 animals under normal diet and between 20 and 26 wks of age were categorized into a normal or a steatosis phenotype, depending on whether they presented none to mild lipid droplet accumulation or moderate to severe fatty liver, respectively ([supplementary fig. S13, Supplementary Material](#) online). Up to 41.3% of the animals displayed hepatic steatosis without significant differences across lines, sexes, and genotypes except for line 7 females, in which steatosis was more prevalent among the homozygous carriers of the 990G allele when compared with the homozygotes for the R990 allele (Pearson's chi-squared test, $P < 0.0033$; [supplementary data set S10, Supplementary Material](#) online). Subsequently, biopsies of visceral and subcutaneous fat from the same animals were used to investigate potential differences in the adipocyte diameter and size distribution between genotypes. When analyzing animals without hepatic steatosis, homozygotes for the 990G allele displayed a clear pattern toward significantly smaller adipocyte diameters in both lines, sexes, and fat tissues as well as toward

an excess of cells in the smallest size bins ([Fig. 3A and B](#); [supplementary data set S11](#) and [figs. S14 to S17, Supplementary Material](#) online).

To understand these differentiated hepatic and adipocyte phenotypes, RNA was extracted from liver and fat biopsies in animals under a normal dietary condition to analyze the relative expression of genes involved in fat storage, mobilization, and inflammation ([supplementary data set S12](#) and [figs. S18 to S19, Supplementary Material](#) online). In visceral fat from animals without hepatic steatosis (line 7), homozygous carriers of the 990G allele presented significantly lower mRNA expression of the lipolytic adipose triglyceride lipase (ATGL) (Student's t -test $P = 0.029$ in $N = 11$ females including 7 R990 homozygotes and 4 990G homozygotes; $P = 0.014$ in $N = 8$ males including 3 R990 homozygotes and 5 990G homozygotes) when compared with R990 homozygotes, whereas homozygous females for the 990G allele also showed significantly lower peroxisome proliferator activating receptor gamma (PPAR γ) mRNA expression ($N = 11$ including 7 R990 homozygotes and 4 990G homozygotes, Student's t -test $P = 0.036$; [Fig. 3C](#)). Even if not significant, 2 further lipolytic enzymes (i.e. the hormone-sensitive lipase [HSL] in 990G homozygous females [$N = 11$ including 7 R990 homozygotes and 4 990G homozygotes, Student's t -test $P = 0.055$] and the adiponectin in 990G homozygous males [$N = 8$ including 3 R990 homozygotes and 5 990G homozygotes, Student's t -test $P = 0.088$]) seem to show marginally lower mRNA expression in the visceral fat from animals with no steatosis when compared with the corresponding R990 genotypes ([supplementary data set S12](#) and [fig. S18, Supplementary Material](#) online). In contrast, 990G homozygous females with normal liver displayed higher ATGL mRNA expression in the liver (Student's t -test $P = 0.031$ in $N = 10$ females including 6 R990 homozygotes and 4 990G homozygotes and $P = 0.071$ in $N = 8$ males including 3 R990 homozygotes and 5 990G homozygotes; [supplementary fig. S18, Supplementary Material](#) online).

As for animals with liver steatosis (complete data only in line 15), we note that male homozygous carriers of the 990G allele showed significantly larger adipocyte diameters and sizes than those of the R990 allele in both subcutaneous and visceral fat ([supplementary fig. S17, Supplementary Material](#) online) but also contrasting significant HSL expression differences between genotypes in visceral fat when compared with female homozygous carriers of the 990G allele ([supplementary fig. S19, Supplementary Material](#) online). Finally, no differential gene expression patterns were found between genotypes in subcutaneous fat ([supplementary data set S12, Supplementary Material](#) online), while CaSR gene expression was confirmed in all 3 tissues at the quantitative PCR (qPCR) detection limit without differences between genotypes.

Evaluation of Further Potential Off-Target Effects

To evaluate the possibility of additional off-targets that could affect the phenotypic differences inferred for the R990G polymorphism besides those predicted by the

Table 1 Differential serum biochemistries between CaSR R990G genotypes

Both lines	Both sexes			Females			Males		
	990G (N = 64)	R990 (N = 56)	990G (N = 33)	R990 (N = 24)	990G (N = 31)	R990 (N = 32)	990G (N = 31)	R990 (N = 18)	R990 (N = 18)
Calcium (mg/dL)	8.914 ± 0.268	9.015 ± 0.261	8.950 ± 0.237	8.955 ± 0.214	8.876 ± 0.297	9.060 ± 0.286	8.876 ± 0.297	8.882 ± 0.292	9.058 ± 0.292
Phosphorus (mg/dL)	6.407 ± 1.333	6.015 ± 1.374	6.169 ± 1.276	6.428 ± 1.551	6.660 ± 1.366	5.705 ± 1.155	6.660 ± 1.366	6.589 ± 1.286	5.815 ± 1.042
Cholesterol (mg/dL)	99.034 ± 20.054	105.027 ± 20.379	84.652 ± 11.603	92.829 ± 17.625	114.345 ± 15.204	114.175 ± 17.459	114.345 ± 15.204	113.856 ± 18.329	108.939 ± 18.329
HDL (mmol/L)	1.736 ± 0.425	1.921 ± 0.363	1.489 ± 0.234	1.736 ± 0.352	2.000 ± 0.426	2.060 ± 0.309	2.000 ± 0.426	1.924 ± 0.523	2.009 ± 0.351
LDL (mmol/L)	0.307 ± 0.055	0.346 ± 0.076	0.293 ± 0.052	0.337 ± 0.084	0.323 ± 0.056	0.354 ± 0.070	0.323 ± 0.056	0.325 ± 0.052	0.328 ± 0.052
Line 7	990G (N = 39)	R990 (N = 30)	990G (N = 21)	R990 (N = 12)	990G (N = 18)	R990 (N = 18)	990G (N = 18)	990G (N = 13)	R990 (N = 14)
Calcium (mg/dL)	8.917 ± 0.231	9.011 ± 0.260	8.947 ± 0.163	8.940 ± 0.193	8.882 ± 0.292	9.058 ± 0.292	8.882 ± 0.292	8.869 ± 0.316	9.064 ± 0.289
Phosphorus (mg/dL)	6.335 ± 1.211	6.079 ± 1.065	6.112 ± 1.128	6.474 ± 1.014	6.589 ± 1.286	5.815 ± 1.042	6.589 ± 1.286	6.757 ± 1.517	5.563 ± 1.313
Cholesterol (mg/dL)	97.703 ± 21.891	101.067 ± 21.152	83.857 ± 13.335	89.258 ± 20.170	113.856 ± 18.679	108.939 ± 18.329	113.856 ± 18.679	115.023 ± 9.099	120.907 ± 14.169
HDL (mmol/L)	1.675 ± 0.455	1.844 ± 0.391	1.462 ± 0.241	1.598 ± 0.318	1.924 ± 0.523	2.009 ± 0.351	1.924 ± 0.523	2.105 ± 0.210	2.126 ± 0.241
LDL (mmol/L)	0.309 ± 0.059	0.323 ± 0.057	0.295 ± 0.061	0.317 ± 0.066	0.325 ± 0.052	0.328 ± 0.052	0.325 ± 0.052	0.321 ± 0.062	0.387 ± 0.078
Line 15	990G (N = 25)	R990 (N = 26)	990G (N = 12)	R990 (N = 12)	990G (N = 13)	R990 (N = 14)	990G (N = 13)	990G (N = 13)	R990 (N = 14)
Calcium (mg/dL)	8.910 ± 0.324	9.021 ± 0.267	8.955 ± 0.340	8.971 ± 0.240	8.869 ± 0.316	9.064 ± 0.289	8.869 ± 0.316	8.869 ± 0.316	9.064 ± 0.289
Phosphorus (mg/dL)	6.519 ± 1.523	5.940 ± 1.682	6.262 ± 1.552	6.381 ± 1.999	6.757 ± 1.517	5.563 ± 1.313	6.757 ± 1.517	6.757 ± 1.517	5.563 ± 1.313
Cholesterol (mg/dL)	101.112 ± 17.017	109.596 ± 18.819	86.042 ± 8.064	96.400 ± 14.658	115.023 ± 9.099	120.907 ± 14.169	115.023 ± 9.099	115.023 ± 9.099	120.907 ± 14.169
HDL (mmol/L)	1.831 ± 0.360	2.010 ± 0.313	1.534 ± 0.224	1.874 ± 0.342	2.105 ± 0.210	2.126 ± 0.241	2.105 ± 0.210	2.105 ± 0.210	2.126 ± 0.241
LDL (mmol/L)	0.305 ± 0.051	0.373 ± 0.087	0.288 ± 0.031	0.357 ± 0.098	0.321 ± 0.062	0.387 ± 0.078	0.321 ± 0.062	0.321 ± 0.062	0.387 ± 0.078

For each group and metabolite, mean concentrations per genotype are given with the standard deviation. Significance between genotypes was evaluated by means of a factorial ANOVA (considering genotype, sex, and line when applicable) or a 1-way ANOVA when just evaluating differences among genotypes within a given sex in a line. In bold, *P*-values < 0.05; 990G, homozygous carriers of the derived allele; R990, homozygous carriers of the ancestral allele.

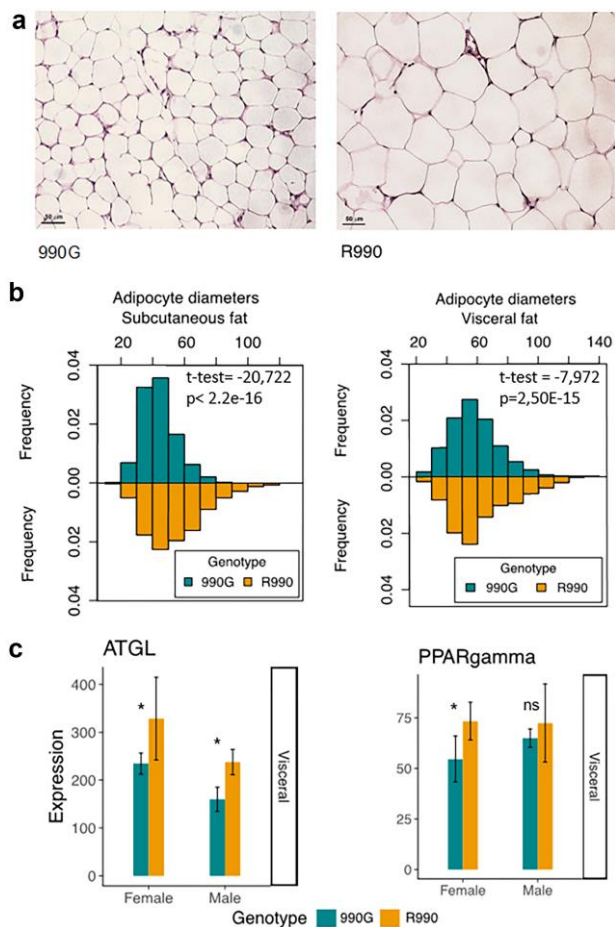


Fig. 3. Differential adipose tissue features between CaSR R990G genotypes. **a**) Visceral fat histology differences between genotypes in hematoxylin and eosin staining. Right: the histology of a 990G female homozygous (22 wks). Left: the histology of a 990R female homozygous (23 wks). **b**) Adipocyte diameters (μm) in subcutaneous and visceral fat. Differences between genotypes were tested through a *t*-test ($N = 11$ females from line 7, including 5 990G homozygotes and 6 R990 homozygotes, respectively). **c**) Differential ATGL and PPAR γ gene expression between genotypes in visceral fat ($N = 11$ females from line 7, including 4 990G homozygotes and 7 R990 homozygotes for ATGL, and 4 990G homozygotes and 6 R990 homozygotes for PPAR γ ; $N = 8$ males from line 7, including 5 990G homozygotes and 3 R990 homozygotes for both ATGL and PPAR γ). * $P < 0.05$; ns, nonsignificant. Relative expression is represented per 1,000 copies of Actin.

Benchling gRNA designing tool, we generated whole-genome sequences (WGS) at 22.2 \times for 15 F2 animals (including 4 R990 and 3 990G homozygotes from line 7 plus 4 R990 and 4 990G homozygotes from line 15; see details in [supplementary note S2](#) and [note S2 tables SN1 to SN9](#), [Supplementary Material](#) online). Since the 2 CaSR lines phenotyped here were established using animals deriving from CBA and B6 strain backgrounds, we retained as potential off-target sites those that were found across the F2 sequenced individuals while being absent in the CBA and B6 strain references available from the Mouse Genome Project ([Keane et al. 2011](#)). Among these, we found no functional variant following the same genotype patterns of the R990G polymorphism within any of the

2 lines. Thus, no potential off-targets (or background variants) seem to be directly influencing the phenotypic differences described above when comparing R990 and 990G homozygotes within each line. However, when analyzing those variants specific to the F2 data set showing differences between lines (when comparing 7 line 7 and 8 line 15 F2 animals), we identified 27 potential off-target (or background) polymorphic sites within line 7 and up to 52 of them segregating within line 15. Five of these putative line-specific off-targets were potentially functionally relevant and found on genes either highly expressed in the fat pads and/or somehow related to fat metabolism (see details in [supplementary note S2](#), [Supplementary Material](#) online). Consequently, they could be influencing some of the differential features observed between the 2 lines such as the greater adiposity detected in both R990 and 990G line 15 individuals. Despite the presence of such putatively line-specific off-target sites, those phenotypic differences observed when comparing R990 and 990G homozygotes within each line are more likely driven by the R990G variant itself.

Discussion

After identifying the R990G substitution in the CASR gene as a putative adaptive variant in the Andamanese to follow-up, we first used genomic data to investigate whether other SE Asian hunter-gatherer groups presenting the DSWS phenotype shared the same accompanying signatures of recent positive selection and high prevalence of this nonsynonymous polymorphism. No unusual patterns of genetic variation were found in Papuan New Guinea, but hunter-gatherer groups from Malaysia and the Philippines presented significant deviation from neutrality in the CASR flanking gene region and high frequencies for the associated G derived allele at rs1042636 (encoding for 990G). The lowest 990G allele frequencies within Malaysia and Philippines were found in the Temiar and the Batak, both populations previously recognized to have received gene flow from other neighboring populations ([Fix 1995](#); [Scholes et al. 2011](#)). In turn, the Temiar also present a more sedentary lifestyle than the Jehai and Kintaq Malaysian groups and a less pronounced DSWS phenotype ([Fix 1995](#); [Deng et al. 2022](#)). Moreover, while only the Andamanese population presented conclusive evidence for moderate selection ($s = 0.0044$) when analyzing the 3 hunter-gatherer groups independently, our analyses indicated a higher likelihood for a scenario of weak selection ($s = 0.0025$) acting on rs1042636 during the last 28,000 yrs when grouping them all. Therefore, we suggest the action of positive selection in the CASR gene to have started between the first settlement of SE Asia (~ 50 to 60 kya) and the western and eastern Neolithic migration waves associated with the arrival of the Austroasiatic ($\sim 6,500$ ya) and Austronesian ($\sim 3,000$ ya) languages in Malaysia and Philippines, respectively ([Philip et al. \(2017\)](#)).

Next, we generated a KI mouse for the human R990G substitution and assessed its phenotypic impact by

exploring for potential differences between the ancestral (R990) and derived (990G) homozygous sibling carriers resulting from several heterozygous crosses within 2 independent R990G KI mouse lines. As expected for an activating CaSR mutation, the derived allele of the R990G (rs1042636) polymorphism is known to be significantly associated with lower serum Ca in healthy humans (Kanai et al. 2018). Here, we found a significant association of the 990G homozygous genotype with lower serum Ca mainly in males. Assuming in mice the same effect size on serum Ca concentrations described in humans for the rs1042636 polymorphism (Kanai et al. 2018), the chance for detecting an association with a P -value < 0.05 was 84.06% in the whole mice group ($N = 120$) and 52.37% in the female group ($N = 57$). Thus, we probably had too small sample sizes to fully recapitulate the expected hypocalcemia phenotype of the R990G substitution. However, the clearest differential phenotype found in our R990G KI mouse model was the higher weight of the homozygous carriers of the 990G allele, which, at least in females, was accompanied by a tendency toward presenting higher BMI, higher fat, and lower lean body content. Interestingly, Ca supplementation in the diet has been shown to elicit significant body weight loss and body fat content in mice and rats (Sun et al. 2012; Zhang et al. 2018). Similarly, supplementation of dietary Ca in humans has been suggested to reduce the body weight of children and adults (Heaney et al. 2002; Li et al. 2016) and the abdominal visceral adipose depots in overweight and obese adults (Rosenblum et al. 2012). On the contrary, rats fed with low-Ca diets not only showed a greater visceral fat mass and CaSR expression in white adipose tissue but also lower serum fatty acids and glycerol concentrations than normal Ca-fed rats (He et al. 2011). Thus, our finding of greater body weight and fat content in 990G homozygotes which, as we have shown, display a tendency toward lower serum Ca when compared with homozygous R990 animals is consistent with results from previous studies (Heaney et al. 2002; He et al. 2011; Li et al. 2016).

The antiobesity effects of dietary Ca have been suggested to result from the direct role of Ca in modulating fat metabolism (Zhang et al. 2019) with intracellular Ca having a key role in regulating lipid metabolism and triglyceride storage in adipocytes (Zemel 2002). In agreement with these observations, distinct systemic and molecular accompanying phenotypes related to lipid handling and adipose tissue homeostasis were further observed in our KI mouse model. These included differential cholesterol, HDL, and LDL serum concentrations, as well as contrasting adipocyte sizes and expression of lipolytic genes (i.e. *ATGL* and *PPARG*) between the homozygous mice carriers of the ancestral (R990) and the derived (990G) alleles of the R990G substitution. We also found that the presence of a fatty liver somehow conditioned the direction of the effects of the R990G substitution on adipocyte size and specific gene expression patterns in the visceral adipose tissue, the latter with some differences between sexes. Although under an excess of hepatic fat accumulation we observed

some expected effects resulting from the activation of CaSR associated with obesity (i.e. larger adipocyte sizes and hypertrophy), we suggest that the putative adaptive role of the R990G substitution in hunter-gather human groups presenting the DSWS phenotype is probably determined in a physiological environment of no pathological accumulation of fatty acids. Moreover, the higher preadipocyte differentiation (Bravo-Sagua et al. 2016) and the antilipolytic effects (He et al. 2012) known to happen upon activation of CaSR could explain many of the differential lipidic and adipose features found associated with the 990G genotype in our study. Within this context, we propose that the smaller adipocyte sizes observed in the 990G homozygous carriers with no hepatic steatosis could result from an early mitogenic effect of CaSR activation in preadipocytes. Such an effect could lead to the maturation of a higher number of adipocytes, providing greater fat storage capacity and leading to the higher body weight and BMI observed in the 990G homozygotes. In contrast, 990G homozygous carriers with hepatic steatosis displayed a clear tendency toward greater adipocyte cell sizes and adipocyte hypertrophy. As in obesity, in these animals, the maximum adipocyte capacity to store an excess of fatty acids as triglycerides in lipid droplets is probably being reached and, as a result, fatty acids start accumulating in the liver, among other nonadipose tissues. We did not detect, however, a clear pattern of differential expression of inflammatory or lipogenic genes associated with the R990G substitution. In rats fed with low-Ca diets, CaSR was suggested to affect fat accumulation via antilipolytic pathways (He et al. 2011) and in vitro experiments demonstrated that the decreased expression of the 2 main lipolytic enzymes (i.e. HSL and ATGL) in SW872 adipocytes because of CaSR expression stimulation was attained by increasing the intracellular Ca and reducing the cAMP levels (He et al. 2011). In accordance with this antilipolytic effect of CaSR activation, our results clearly show that male and female 990G homozygous carriers with normal liver present significantly lower ATGL mRNA expression in visceral fat. This result is also compatible with the observation that the human polymorphism rs1042636 causes a reduction of at least 20% of the lipolysis in omental adipose tissue (Reyes et al. 2012). Additionally, we also detected that the female homozygotes for the 990G allele presented significantly lower expression of PPAR γ , which is in accordance with the lower mRNA expression of lipolytic genes observed in that genotype. Moreover, a metabolic link has been suggested between the lipolytic activity of adipocytes and the rate of cellular efflux to HDL (Verghese et al. 2007). Thus, the lower cholesterol levels observed in the homozygous carriers of the 990G allele could be reflecting the corresponding attenuation of lipolysis resulting from the lower visceral adipocyte expression of ATGL (and probably also HSL). However, despite all the data compiled, further experimental work will be required to fully understand the mechanistic links by which the R990G substitution causes these observed differential phenotypic features.

Additional limitations of the present study must be acknowledged. First, despite the widespread use of the mouse as a fair experimental model to study biological processes and diseases in humans, our different physiologies and anatomies might limit the mouse model applicability to accurately recapitulate individual human adaptive phenotypes. Secondly, although during the CRISPR-Cas9 editing experiment different strategies were applied to minimize the possible off-target effect, such as ribonucleoprotein (RNP) in situ electroporation directly into 1-cell zygotes and the use of an asymmetric vector, the 2 lines deriving from 2 independent KIs displayed some phenotypical differences between them. Although no modifications were detected when sequencing the off-target loci predicted by the Benchling tool used for the 2 gRNA design (see [Materials and Methods](#)), we recognize that other rare off-target events could still occur ([Atkins et al. 2021](#)). Additionally, other background genetic differences could have been introduced within each line initial crosses. Indeed, when analyzing WGS for a subset of F2 individuals, we detected a few putative new functional variants differentiating the 2 lines but none following the same genotype patterns of the R990G substitution. Thus, the phenotypic differences observed when comparing the R990 and 990G homozygotes within each line (and specially when replicating across lines, such as the differential body weight and adipocyte sizes) can more likely be attributed to the R990G substitution. However, we cannot reject that some of the phenotypes described here for R990G could be dependent on the genetic background of our line crosses, which could explain the incomplete penetrance sometimes observed across lines and sexes. In fact, a subset of the putatively line-specific variants identified when comparing 7 line 7 and 8 line 15 F2 individuals were found in genes that are highly expressed in adipose tissue and/or known to have a role in lipid metabolism. In turn, this dependence on the genetic background may have implications for how these phenotypes present in human populations where this polymorphism segregates. Finally, we do not exclude mild phenotypic effects of the R990G substitution in the bone, skin, or other tissues that could not be retrieved in this study due to the sample size of the analyzed mice cohort.

While the 990G allele is found at intermediate frequencies in several populations from East Asia (i.e. 56.7% in Southern Han Chinese [CHS], 53.8% in Japanese in Tokyo [JPT], and 52.4% in Han Chinese in Beijing [CHB]), we note that the *CASR* gene region displays putative signatures of positive selection only in some hunter-gatherer groups from SE Asia, where the polymorphism reaches its highest frequencies (i.e. 87.5% in Andamanese, 96.9% in the Philippine Aeta, and 83.3% in the Malaysian Kintaq). The availability of larger sample sizes and the use of further elaborated demographic models for these populations will probably help to better distinguish the signatures of positive selection postulated here from potential founder and demographic effects. In turn, whereas the physiological consequences we describe for this

nonsynonymous polymorphism are expected in all its carriers, these differences may have been selectively beneficial only under the environmental conditions, lifestyle, and genomic background of the SE Asian populations displaying the DSWS phenotype. Therefore, R990G cannot be inferred to provide a universal advantageous phenotype to all its carriers and it cannot be used either to infer their ancestry. We propose that the differential adiposity profile and higher body weight associated with the R990G substitution in *CaSR* could have been positively selected in hunter-gatherer groups from SE Asia to facilitate fat storage, increasing survival in periods of food scarcity and low caloric intake in their past. Indeed, adipocyte number is a major determinant for fat mass in human adults ([Spalding et al. 2008](#)) and the lower expression of lipolytic genes in visceral adipose tissue might further favor adiposity preventing an unnecessary rapid mobilization of lipids under fasting or exercise conditions ([Nielsen et al. 2014](#)).

We further speculate that the distinct lipid handling features and differential adipose tissue homeostasis caused by R990G could also contribute to some features of the DSWS phenotype such as short stature by advancing puberty or even steatopygia. Anthropometric studies show that fat percentage in the human body increases during puberty, especially in the central region of the female body, leading to an increase in leptin secretion, which regulates menarche inducing both the pubertal growth spurt and the growth plate fusion in the epiphysis ([Siervogel et al. 2003](#); [Lassek and Gaulin 2007](#); [Miranda et al. 2014](#)). Furthermore, the onset of sexual maturation is a plastic mechanism with which humans react to stressful environments in populations from central Europe and the Americas ([Coall and Chisholm 2003](#)) as well as in population groups presenting the DSWS phenotype ([Stock and Migliano 2009](#)). Only the appropriate collection of life trait information and subsequent R990G association testing in the SE Asian hunter-gatherer populations analyzed would allow to test whether the present results support the hypothesis that the low life expectancy of the hunter-gatherer human groups presenting the DSWS phenotype has selected for early maturity and reproduction over physical growth to enhance fertility ([Walker et al. 2006](#); [Migliano et al. 2007](#); [Migliano et al. 2013](#)). While providing further understanding of the adaptive role of the R990G substitution and its contribution to the development of the DSWS phenotype in response to local environmental pressures, such future research (nor the results reported here) cannot be used either to justify any kind of marginalization or to provide a biological justification to the *Othering* treat historically reserved for populations with the DSWS phenotype.

Materials and Methods

Signals of Positive Selection

SNP genotypes from 10 Andamanese and 10 Indian Irula whole-genome sequences generated at ~15X coverage ([Mondal et al. 2016](#)), and 9 unrelated YRI whole-genome sequences from the Complete Genomics data set

(Drmanac et al. 2010) were merged and curated by removing any SNP which had missing data for any individual and subsequently phased with SHAPEIT (Delaneau et al. 2012) using the 1,000 G Project Phase 1 samples as reference. Tests of positive selection based on the site frequency spectrum (Tajima's D, Tajima 1989, and Fay and Wu's H, Fay and Wu 2000) and on comparing the extended haplotype homozygosity profiles between populations (XP-EHH; Sabeti et al. 2007) were then genome-wide calculated in the Andamanese as in Mondal et al. (2016). Tajima's D (Tajima 1989) and Fay and Wu's H (Fay and Wu 2000) were calculated using 3 kb windows, whereas XP-EHH (Sabeti et al. 2007) comparing Andamanese versus Yoruba and Andamanese versus Irula was calculated by SNP.

To identify any putative adaptive variant in the *CASR* gene region, we then used ANNOVAR (Wang et al. 2010) to functionally annotate all SNPs presenting allele frequencies differences >0.25 when comparing the JAR and ONG populations to 6 mainland Indian populations, including Uttar Pradesh Upper Caste Brahmins (UBR), Rajput (RAJ), Vellalar (VLR), Irula (ILA), Birhor (BIR), and Riang (RIA) available from Mondal et al. (2016). We also explored the allele frequencies for the R990G substitution and signals of positive selection along the *CASR* gene region in other SE Asian populations for which phased whole genomes obtained with the 10× technology were available (European Genome-phenome Archive [EGA] study accession number EGAS50000000044). These included several population groups presenting the DSWS phenotype from the Philippines (Aeta $2N = 32$, Batak $2N = 24$, Agta $2N = 20$, Mamanwa $2N = 12$) and Malaysia (Jehai $2N = 18$, Kintaq $2N = 12$, Temiar $2N = 12$) as well as different Indigenous groups from Papua New Guinea (Koinambe $2N = 24$, Sepik $2N = 4$, Kosipe $2N = 20$, Papua New Guinea Highlands $2N = 4$, Australia $2N = 4$). Haplotype composition and structure was explored with Haploview 4.1 (Barrett et al. 2005) using phased data from the Malaysian, Philippine, Papuan New Guinean (considering only the Kosipe and Koinambe groups), and the Andamanese populations analyzed here as well as data from mainland India and the Han Chinese population from the 1000 G Project (CHB). For all 3 SE Asian groups, we applied a test of positive selection based on the site frequency spectrum (SF select; Ronen et al. 2013) available at <https://github.com/rronen/SFselect> following the same procedure as in Walsh et al. (2020) and computed the XP-EHH statistic (Sabeti et al. 2007) comparing the Philippines and the Malaysian population groups to the Papua New Guinea group, with the rehh 2.0 program (Gautier et al. 2017). For each selection test and population group, z-scores across the *CASR* gene region were computed from the mean and standard deviation of the genome-wide raw values of each corresponding statistic (supplementary data set S1, Supplementary Material online). To test for selection and estimate the past allele frequency trajectory and selection coefficient of the candidate SNP rs1042636 (chr3:122003769, GRCh37/hg19), we first inferred genome-wide gene genealogies

with Relate (Speidel et al. 2019) and then applied the CLUES algorithm (Stern et al. 2019). For that, we incorporated additional phased samples to the SE Asian data set including 8 samples from India (Irula $2N = 6$, Birhor $2N = 4$, Madiga $2N = 2$, and Riang $2N = 4$) and 16 samples from various Asian populations (Ami $2N = 4$, Dusun $2N = 4$, Han $2N = 4$, She $2N = 2$, Burmese $2N = 2$, Japanese $2N = 2$, Thai $2N = 2$, Igorot $2N = 4$, Balochi $2N = 2$, Cambodian $2N = 2$, Kinh $2N = 2$, Miao $2N = 2$), as well as 2 European and 4 African samples (CEU and YRI from the 1,000 Genomes Project). We converted the phased VCF file to the .haps and .sample formats using the RelateFileFormats tool (`-mode ConvertFromVcf`) for the entire data set, which consisted of 132 samples. We then used the PrepareInputFiles.sh module, which requires an ancestral genome (human_ancestor_GRCh37_e59) to polarize variants as ancestral or derived, and a strict callability mask (GRCh37) to retain only SNP positions with high variant calling certainty in our sequence data. To build the tree, we ran RelateParallel.sh using the HapMap build GRCh37 genetic map and options `-m 1.25e-8` and `-N 30000`. To visualize the local genealogical tree for the target variant, we utilized the TreeViewMutation.sh module. We employed RelateExtract (`-mode SubTreesForSubpopulation`) to generate 4 subtrees for the Andamanese ($N = 10$), Philippines ($N = 42$), Malaysia ($N = 24$), and a combined group of all 3 populations ($N = 76$) and then estimated the coalescence rate over time using the EstimatePopulationSize.sh module for each of these 4 subtrees. We used a mutation rate of 1.25×10^{-8} , a generation time of 28 yrs, 5 iterations, and a tree dropping threshold of 0.5. After estimating the branch lengths for each subtree using the SampleBranchLengths.sh module with the `--format b` option, we separately ran CLUES on the 4 local trees to estimate the derived allele frequency trajectory over time for the locus of interest. Finally, we generated a plot of the trajectory using the plot_traj.py script.

Guide RNA Design and Cas9 Assay for Guide RNA Efficiency

To generate the *CaSR* R990G substitution, 2 guide RNAs (gRNAs) were designed using the Benchling design tool (www.benchling.com). They were selected to have the highest score for both the off-target and on-target sites and to have a cleavage site as close as possible to the targeted nucleotide (see details in supplementary fig. S6, Supplementary Material online). The resulting gRNAs sequences were as follows: 5'-CGGGAAGTCCATGCC CCAGA-3' and 5'-ACGGGAAGTCCATGCCAG-3'. To test gRNA efficiency, a substrate DNA was first created by subcloning *Casr* exon 7 from mice into a Zero-Blunt cloning vector (Invitrogen) and a Cas9 cleavage assay was subsequently performed for each gRNA (see supplementary fig. S20, Supplementary Material online). Vectors were linearized and purified. To assay cleavage, a total of 300 nM of a 1:1 (vol/vol) mix of crRNA

and tracrRNA was incubated for 5 min at 75 °C and subsequently allowed to cool to room temperature. One μL of Cas9 nuclease (3 $\mu\text{g}/\mu\text{L}$), 3 μL of NEB Cas9 buffer, and 11 μL of H_2O were then added to the mix and incubated for 10 min at 25 °C to allow the formation of the RNP complex. Five μL of substrate DNA (30 nM) was then added to the solution and incubated for 1 h at 37 °C. Cleavage products were subject to agarose gel electrophoresis, and the efficiency of the gRNA was measured by the ability to efficiently cleave substrate DNA.

Electroporation of CRISPR RNPs and Homology-Directed Repair Template into Zygotes

A donor template for homology-directed repair (HDR) was designed according to guidelines (Richardson et al. 2016) to generate the R990G substitution and purchased from Integrated DNA Technologies (IDT). For gRNA annealing, 10 μL (at 54 ng/ μL) crRNA plus 15.6 μL (at 84 ng/ μL) tracrRNA were incubated for 10 min at 75 °C followed by gradual cooling to room temperature. Subsequently, 17.94 μL of the gRNA annealing reaction was incubated for 10 min at 25 °C with 5.42 μL (at 125 ng/ μL) of Cas9 nuclease, after which 32.5 μL (at 500 ng/ μL) of ssDNA R990G template plus 74.14 μL OPTIMEM were added. Forty μL of this solution (assembly reaction) were aliquoted to be used for the electroporation. Four-week-old B6CBAF1/J female mice were superovulated with 5 IU of PMSG and 5 IU hCG and were subsequently mated with male C57B6/J stud mice. Zygotes were harvested at stage E0.5. Electroporation was then carried out with a NEPA21 electroporator (NEPAgene) using the following conditions: assembly solution-containing zygotes, 40 μL ; poring pulse, 250 V; length, 1.5 ms; interval, 50 ms; decay rate, 10; number of pulses, 4; transfer pulse, 20 V; length, 50 ms; interval, 50 ms; decay rate, 10; and number of pulses, 5. Following electroporation, surviving zygotes were transferred into 6-wk-old CD1 recipient females via oviduct transfer. Seventeen offspring were obtained, and 8 of them tested positive for the R990G substitution after PCR-RFLP analysis (supplementary table S2, Supplementary Material online). All animal handling and experimental procedures conducted at the Mouse Mutant Core Facility (Institute for Research in Biomedicine [IRB]) were approved by the Ethical Committee of the Parc Científic de Barcelona (project 19-013-9170PRO-SPF).

Genomic DNA Extraction

Genomic DNA was extracted from tail or ear biopsies of 2-wk-old mice by a standard proteinase K and isopropanol-based method. For that, samples were incubated overnight at 55 °C in 500 μL of lysis buffer and 7.5 μL of proteinase K. The solution was then centrifuged for 5 min at 18,000 $\times g$, and the resulting supernatant was transferred into another tube, where 500 μL of isopropanol were added. We subsequently processed the solution by inverting the tube 5 to 6 times and by centrifuging it at 18,000 $\times g$ for 10 min. Isopropanol was

then removed and the pellet was washed twice with ethanol 70% at -20 °C followed by 5 min of centrifugation at 18,000 $\times g$. Finally, purified DNA was resuspended in 300 μL of TE and incubated for 1 h at 65 °C in agitation.

R990G Genotyping

Since the R990G substitution generates a consensus sequence for the *BtgI* restriction enzyme, we genotyped all newborn mice by PCR-RFLP analysis (see supplementary fig. S6, Supplementary Material online). To do so, *Casr* exon 7 genomic DNA was amplified using forward and reverse primers 5'-AACACCATCGAGGAGGTGC-3' and 5'-CTCCACCGCTGATGACGAAG-3', respectively. PCR reactions were performed in a volume of 50 μL containing 1 \times KOD-HS buffer, dNTPs (200 μM final), Mg^{2+} (1.5 mM final), 2 μL of forward primer (400 nM final), 2 μL of reverse primer (400 nM final), 0.5 μL KOD Hot Start DNA polymerase (1 unit), and 1 μL of purified DNA (100 to 250 ng/ μL). PCR conditions were 1 cycle of initial denaturation at 95 °C for 3 min; 40 cycles of denaturation at 95 °C for 30 s, primer annealing at 60 °C for 20 s and extension at 70 °C for 20 s, and final extension at 70 °C for 5 min. After amplification, PCR products were run on agarose gels, purified with GeneJET Gel Extraction Kit (Thermo Fisher Scientific), and subsequently incubated for 90 min at 37 °C with the *BtgI* enzyme (BioLabs) following manufacturer's instructions.

Editing Efficiency and Quality

To evaluate the efficiency and quality of the editing, we cloned the amplified PCR products from each positive mouse into a pCR-Blunt vector (Invitrogen) following the manufacturer's conditions. A total of 24 colonies from each founder were analyzed. Plasmid DNA was amplified and subject to RFLP analysis with *BtgI*. DNA from each colony was then extracted using PureLink Quick Plasmid Miniprep Kit (Thermo Fisher Scientific) and subsequently used for PCR-RFLP analysis as previously described to verify CRISPR editing efficiency. Up to 4 colonies from each confirmed positive mosaic were then Sanger sequenced to ensure the correct editing of the R990G substitution and discard any potential insertions or deletions introduced during the CRISPR-Cas9 editing protocol. Five of the 8 mosaic mice carried the expected sequence around the edited site (supplementary table S2, Supplementary Material online).

Establishment of 2 Lines and Animal Experimental Procedures

Mosaic founder mice generated at the Mouse Mutant Core Facility (IRB) and harboring the corrected edited position were then bred with CBA mice (6 wks) from Charles River Laboratories (France) to generate founder lines at the Barcelona Biomedical Research Park (PRBB) animal facility. All 5 correctly edited mosaic mice transmitted the substitution to their offspring after breeding with CBA mice. We selected 1 mosaic founder deriving from each separate editing experiment and gRNA to establish 2 independent

CaSR R990G mice lines, denoted as lines 7 and 15, by crossing the corresponding heterozygote descendants from the F1 generation. Genotyping was performed by PCR-RFLP analysis after extracting DNA from either tail or ear biopsies obtained just after weaning as described above. After establishing 17 crosses between heterozygous individuals in the line 7 F1 and 9 crosses between heterozygous individuals in the line 15 F1, a total of 125 F2 mice in line 7 and 90 F2 mice in line 15 were used for experimental procedures (see [supplementary fig. S7, Supplementary Material](#) online). Thus, all phenotyped animals in this study belonged to the filial generation 2 (F2) to minimize the drift effect of inbreeding across several generations.

Potential off-target sites for each corresponding gRNAs, as predicted by the Benchling designing tool, were checked by standard Sanger sequencing in all founders for lines 7 (22 mice, 7 off-target sites) and 15 (21 mice, 11 off-target sites), respectively. Similarly, the correct editing within *Casr* was verified in all F1 founders or corresponding F2 descendants by Sanger using primers 5'-AACACCATCGAGGAGGTG C-3' and 5'-CTCCACCGCTGATGACGAAG-3', respectively. Off-target genes and primers for the amplification and sequencing are shown in [supplementary tables S3 and S4, Supplementary Material](#) online, and the subsequent aligned sequences obtained for all off-targets and the *Casr*-edited region are available in [supplementary data sets S13.1 to S13.20, Supplementary Material](#) online. Moreover, WGS were generated in 15 F2 individuals (at more than $\sim 19.5\times$ coverage) to further evaluate the possibility of additional genome-wide off-targets introduced by the CRISPR-Cas9 editing experiment (see details in [supplementary note S2, Supplementary Material](#) online). Mice for phenotyping were kept under pathogen-free conditions in a controlled temperature and humidity environment with a 12:12 h light:dark cycle and had free access to water and were fed ad libitum on a standard diet (except otherwise indicated) at the PRBB animal facility. A subset of 87 animals (including 42 mice from line 15 and 45 from line 7) were subjected to a vitamin D-deficient diet (Envigo, TD. 89123) from the 3rd to the 14th wk of age. All animal handling and experimental procedures for the phenotyping were conducted in accordance with the European Union Directive 2010/63/EU and the Spanish Legislation (Real Decreto 53/2013, BOE 34: 11370-11421) and were approved by the Ethical Committee of Animal Experimentation of the PRBB (project PML-18-0014) and the Animal Research Committee of the Department of Territory and Sustainability, Generalitat de Catalunya, Spain (project 10043).

Blood and Urine Biochemical Analysis

Blood samples were collected from the retro-orbital vein at the 14th wk of age and left to rest for 30 min. Serum was then separated by centrifugation at $2,000\times g$ for 10 min at 4 °C, aliquoted conveniently, and stored at -20 °C until further analysis. Serum samples were analyzed for Ca, magnesium, phosphorus, creatinine, fructosamine,

triglycerides, nonesterified fatty acids (NEFAs), total cholesterol, HDL, and LDL on an automated clinical chemistry analyzer Olympus AU400. Serum PTH and osteocalcin concentrations were measured using the Mouse PTH 1 to 84 ELISA Kit (Immutopics) and the Mouse Osteocalcin EIA Kit (Alfa Aesar), respectively, following the manufacturer's protocols. Urine samples were collected from mice housed in metabolic cages at around 13 wks of age. After 48 h, 24 h urine was collected from each animal and rapidly stored at -20 °C until further analysis. Urinary Ca, inorganic phosphate (Pi), and creatinine were measured on an automated clinical chemistry analyzer Olympus AU400. All blood and urine biochemical analyses were determined at the Servei de Bioquímica Clínica Veterinària, Universitat Autònoma de Barcelona (Cerdanyola del Vallès, Barcelona).

Body Weight Growth Curves and BMI

Body weight changes were recorded from wks 3 to 20 and examined weekly between lines, sexes, and genotypes using factorial ANOVAs. Since several experimental procedures (such as blood extraction, use of metabolic cages for urine collection, and transport and anesthetics for the micro-CT analysis performed outside the PRBB animal facility) could be affecting unevenly numbers of individuals across the studied groups, we also applied a mixed-model ANOVA with repeated measures along wks 4 to 12 to analyze the overall effect of the examined variables before performing any of the aforementioned experimental procedures. Body weight and crown rump length were recorded at the final point (between wks 20 and 26) for 128 animals. The BMI was calculated as the ratio between body weight (g) and square crown rump length (mm). Weight, crown rump length, and BMI among experimental groups were subsequently normalized by age. Power calculations for the sample sizes and statistical tests used (here and in the phenotyping analysis below) were obtained with the Power T Z Calculator tool (https://www.statskingdom.com/32test_power_t_z.html) after considering a 2-sample *t*-test ($H_1: \mu = \mu_0$) and a significance level $\alpha = 0.05$ (see details in [supplementary data set S14, Supplementary Material](#) online).

Body Composition Analysis and Micro-Computed Tomography

Body composition analyses were performed at 14 wks of age at the Animal Facility of the Parc Científic de Barcelona (PCB) within the PCB-PRBB Animal Facility Alliance. Fat and lean body mass of nonanesthetized live mice were determined using the EchoMRI Analyzer system (Echo Medical Systems, Houston, TX, USA). For ex vivo micro-CT analysis, femur and tibia bones were isolated at the final point (25 wks of age), fixed in PFA 4% overnight at 4 °C, washed in PBS, and then stored in PBS at 4 °C. The bone micro-architecture of the tibial cortical bone and the trabecular bone at the proximal tibial metaphysis were assessed using a Perkin Elmer Quantum Fx instrument at the

Preclinical Imaging Platform of the Lab Animal Service of the Vall d'Hebron Institut de Recerca (VHIR).

Histopathological Analyses

Skin biopsies and liver, kidney, and thyroid gland samples obtained at the terminal point were fixed in 10% buffered formaldehyde, dehydrated in increasing concentrations of ethanol, and embedded in paraffin wax. Tissue samples were subsequently sectioned and stained with hematoxylin and eosin for pathological evaluation at the Departamento de Medicina y Cirugía Animal, Facultad de Veterinaria, Universidad Complutense de Madrid.

Wound Healing Experiments and Skin Histology

Skin biopsies were performed after depilation using 5 mm disposable punches on anesthetized mice (line 7). Wound healing was evaluated at a macroscopic level and monitored by taking digital photographs at different time points after the lesion was performed at either 10 (6 mice) or 20 wks (12 mice). At the same time points, the larger and minor diameters of the skin lesions were also manually measured by using a caliper. Wound areas were determined by applying the formula: $(\text{large diameter}/2) \times (\text{minor diameter}/2) \times \pi$, whereas the wound healing rate was then estimated as $[(\text{area of original wound} - \text{area of actual wound}) / \text{area of original wound}] \times 100$. Skin biopsies at 20 wks of age were incubated in paraformaldehyde 4% overnight, paraffin embedded to be cut in 5 μm thickness and then stained with hematoxylin and eosin. Differences in epidermal thickness between genotypes were evaluated using 5 measures per sample and region (derma or epidermis).

Dissection and Histology of Liver and Fat Tissue Samples

Adult animals were sacrificed from the 5th up to the 6th month of their life to retrieve the medial and left liver lobes, inguinal subcutaneous white fat pads, and visceral white fat pads. One-half of each dissected tissue was incubated in RNAlater stabilization solution (Invitrogen) according to the manufacturer's instruction to preserve the RNA of each specimen for gene expression quantification. The other half was incubated for 12 h at 4 °C in paraformaldehyde (4% in PBS); then, paraffin inclusion and hematoxylin and eosin stains were performed by the Histology Unit of the Centre for Genomic Regulation in Barcelona. Twelve- μm -thick slides were produced for each tissue and observed using a Zeiss AxioImager Z1 microscope (Apotome) (Carl Zeiss MicroImaging). Liver biopsies were categorized into a normal or a steatosis phenotype according to the degree of lipid accumulation in sections of the tissue stained with hematoxylin and eosin using as references Figure 1 in Xu et al. (2012) and Figure 4 in Kristiansen et al. (2016). Liver sections presenting normal and mild phenotype with lipid droplets were classified as "normal" and those presenting moderate to severe fatty liver as "steatosis." For each animal, the phenotypic assignment was performed genotype blinded 3 times in 3 independent days. A Pearson's chi-squared test was used to

determine whether there is a statistically significant difference between the expected frequencies and the observed frequencies between the 2 steatosis phenotype categories and the R990G genotypes.

The open-access image analysis software ImageJ was used to calculate cell diameters and areas in both subcutaneous and visceral fat stains from 5 to 7 animals per each sex and genotype. Five to 7 images per animal were analyzed to retrieve most of the tissue's variability. A *t*-test was used to evaluate differences between genotypes within each line and sex. The frequency distribution of fat cell areas was calculated using bins from 0 to 15,000 μm^2 in 500 increments as reported in Parlee et al. (2014). A Pearson's chi-squared test was used to determine differences between genotypes across all bins after collapsing those with expected frequencies < 5. Analyses were performed separating animals with normal liver and hepatic steatosis.

RNA Extraction and qPCR

Total RNA was extracted from liver and adipose tissue specimens following the standard protocol of the higher purity tissue total RNA purification kit (Canvax, Cordoba, Spain). RNA quality and quantity were analyzed using a NanoDrop spectrophotometer (NanoDrop Technologies, Wilmington, DE, USA). DNase treatment was performed on 300 ng of total RNA for highly expressed genes and on 1,000 ng of total RNA for genes with low expression using DNase I/RNase-free standard protocol (Thermo Fisher Scientific). The Transcription First Strand cDNA synthesis kit (Roche Diagnostics) was used to perform the reverse transcription reaction. qPCR reactions were performed using the iTaq Universal SYBR Green Supermix (Bio-Rad Laboratories). Amplifications were carried out with an initial denaturation step at 95 °C for 3 min, followed by 44 cycles of 95 °C for 10 s and 57 °C for 1 min. Each qPCR reaction was followed by a melting curve analysis to verify specificity. Subsequently, the expression of 9 genes related to inflammation and lipid metabolism was quantified in the liver and fat samples using the actin housekeeping gene as an internal control (see primer details in [supplementary table S5, Supplementary Material](#) online). In particular, the relative gene expression for ATGL, HSL, PPAR γ , PPAR α , FAS, FABP4/aP2, Tnf-alpha, adiponectin, and LPL was quantified using the $2^{-\Delta\Delta C_t}$ method and given as copies of mRNA per 1,000 copies of actin mRNA. Statistical significance between genotypes was analyzed by the 2-sample *t*-test and ANOVA.

Supplementary Material

[Supplementary material](#) is available at *Molecular Biology and Evolution* online.

Acknowledgments

We especially thank all volunteers providing samples, local contacts, and researchers that made this research possible. We acknowledge the PRBB Animal Facility of the Parc de

Recerca Biomèdica de Barcelona, Yolanda Saco from the Servei de Bioquímica Clínica Veterinària at the Universitat Autònoma de Barcelona, and Juan Antonio Camara from the Preclinical Imaging Platform of the Vall d'Hebron Institut de Recerca for their technical help. We also especially thank Patricia Robledo for providing advice and lending us metabolic cages.

Author Contributions

E.B., B.S., F.J.M., J.B., S.F. and J.M.-C. designed the research; B.S., J.E., J.M., S.A., M.V., and S.F. performed the research; B.S., S.A.B., J.G.-C., B.D., M.M., S.W., G.A., A.B.M., and E.B. compiled and analyzed the data; and B.S. and E.B. wrote the paper with contributions from S.A.B., B.D., S.A., G.A., S.F., A.B.M., J.B., and F.J.M.

Funding

This work was supported by Agencia Estatal de Investigación (AEI, DOI: 10.13039/501100011033), Fondo Europeo de Desarrollo Regional, Ministerio de Ciencia e Innovación, and Ministerio de Ciencia, Innovación y Universidades with project grants BFU2016-77961-P, PID2019-110933GB-I00, and the Unidad de Excelencia María de Maeztu Ref. CEX2018-000792-M; and by Agència de Gestió d'Ajuts Universitaris i de la Recerca, Generalitat de Catalunya (2017SGR00702). B.S. was supported with an FPI-MINECO PhD fellowship (BES-2017-080343). S.A. was supported by Beatriu de Pinós 2017 BP 00176 and by the Serra Hunter Fellowship from Generalitat de Catalunya.

Data Availability

All raw phenotypical data are available as supplementary material ([supplementary data sets S1 to S14](#), [Supplementary Material](#) online). Cryopreserved embryos for the KI mouse lines generated in this study are available upon request. Genomic data from the Andamanese are publicly available (PRJEB11455); genomic data from other SE populations are available under controlled access due to restrictions imposed by ethical approval and the informed consent from participants at the EGA study accession number EGAS50000000044. WGS data from 15 F2 mice have been deposited at the European Nucleotide Archive (ENA) under accession number ERP152557. Sanger sequences generated for all predicted off-targets and the *Casr* region are available in Figshare (https://figshare.com/articles/dataset/CaSR_F2Sanger_Sequencing_results_for_the_off-targets_and_CASR_gene_in_F1_and_F2_generation/23717310). This study did not produce any new methodological algorithm; all codes used are mainly pipelines specialized in running in our cluster, which we will make available upon request.

References

Atkins A, Chung C-H, Allen AG, Dampier W, Gurrola TE, Sariyer IK, Nonnemacher MR, Wigdahl B. Off-target analysis in gene editing and applications for clinical translation of CRISPR/Cas9 in HIV-1

- therapy. *Front Genome Ed.* 2021;**3**:673022. <https://doi.org/10.3389/fgeed.2021.673022>.
- Auton A, Abecasis GR, Altshuler DM, Durbin RM, Abecasis GR, Bentley DR, Chakravarti A, Clark AG, Donnelly P, Eichler EE, et al. A global reference for human genetic variation. *Nature.* 2015;**526**(7571):68–74. <https://doi.org/10.1038/nature15393>.
- Barrett JC, Fry B, Maller J, Daly MJ. Haploview: analysis and visualization of LD and haplotype maps. *Bioinformatics.* 2005;**21**(2): 263–265. <https://doi.org/10.1093/bioinformatics/bth457>.
- Bravo-Sagua R, Mattar P, Díaz X, Lavandero S, Cifuentes M. Calcium sensing receptor as a novel mediator of adipose tissue dysfunction: mechanisms and potential clinical implications. *Front Physiol.* 2016;**7**:395. <https://doi.org/10.3389/fphys.2016.00395>.
- Casillas S, Mulet R, Villegas-Mirón P, Hervas S, Sanz E, Velasco D, Bertranpetit J, Laayouni H, Barbadilla A. PopHuman: the human population genomics browser. *Nucleic Acids Res.* 2018;**46**(D1): D1003–D1010. <https://doi.org/10.1093/nar/gkx943>.
- Chang W, Dvorak M, Shoback D. Assessing constitutive activity of extracellular calcium-sensing receptors in vitro and in bone. *Methods Enzymol.* 2010;**484**:253–266. <https://doi.org/10.1016/B978-0-12-381298-8.00013-7>.
- Chang W, Tu C, Chen TH, Bikle D, Shoback D. The extracellular calcium-sensing receptor (CaSR) is a critical modulator of skeletal development. *Sci Signal.* 2008;**1**(35):1–14. <https://doi.org/10.1126/scisignal.1159945>.
- Coall DA, Chisholm JS. Evolutionary perspectives on pregnancy: maternal age at menarche and infant birth weight. *Soc Sci Med.* 2003;**57**(10):1771–1781. [https://doi.org/10.1016/S0277-9536\(03\)00022-4](https://doi.org/10.1016/S0277-9536(03)00022-4).
- Delaneau O, Marchini J, Zagury JF. A linear complexity phasing method for thousands of genomes. *Nat Methods.* 2012;**9**(2):179–181. <https://doi.org/10.1038/nmeth.1785>.
- Deng L, Pan Y, Wang Y, Chen H, Yuan K, Chen S, Lu D, Lu Y, Mokhtar SS, Rahman TA, et al. Genetic connections and convergent evolution of tropical indigenous peoples in Asia. *Mol Biol Evol.* 2022;**39**(2):msab361. <https://doi.org/10.1093/molbev/msab361>.
- Dong B, Endo I, Ohnishi Y, Kondo T, Hasegawa T, Amizuka N, Kiyonari H, Shioi G, Abe M, Fukumoto S, et al. Calcilytic ameliorates abnormalities of mutant calcium-sensing receptor (CaSR) knock-in mice mimicking autosomal dominant hypocalcemia (ADH). *J Bone Miner Res.* 2015;**30**(11):1980–1993. <https://doi.org/10.1002/jbmr.2551>.
- Drmanac R, Sparks AB, Callow MJ, Halpern AL, Burns NL, Kermani BG, Carnevali P, Nazarenko I, Nilsen GB, Yeung G, et al. Human genome sequencing using unchained base reads on self-assembling DNA nanoarrays. *Science* 2010;**327**(5961):78–81. <https://doi.org/10.1126/science.1181498>.
- Elsholz F, Harteneck C, Muller W, Friedland K. Calcium—a central regulator of keratinocyte differentiation in health and disease. *Eur J Dermatol.* 2014;**24**(6):650–661. <https://doi.org/10.1684/ejd.2014.2452>.
- Enard W, Gehre S, Hammerschmidt K, Hölter SM, Blass T, Somel M, Brückner MK, Schreiweis C, Winter C, Sohr R, et al. A humanized version of Foxp2 affects cortico-basal ganglia circuits in mice. *Cell* 2009;**137**(5):961–971. <https://doi.org/10.1016/j.cell.2009.03.041>.
- Fay JC, Wu C-I. Hitchhiking under positive Darwinian selection. *Genetics* 2000;**155**(3):1405–1413. <https://doi.org/10.1093/genetics/155.3.1405>.
- Fix AG. Malayan paleosociology: implications for patterns of genetic variation among the orang Asli. *Am Anthropol.* 1995;**97**(2): 313–323. <https://doi.org/10.1525/aa.1995.97.2.02a00090>.
- Gautier M, Klassmann A, Vitalis R. rehh 2.0: a reimplementation of the R package rehh to detect positive selection from haplotype structure. *Mol Ecol Resour.* 2017;**17**(1):78–90. <https://doi.org/10.1111/1755-0998.12634>.
- Goltzman D, Hendy GN. The calcium-sensing receptor in bone-mechanistic and therapeutic insights. *Nat Rev Endocrinol.* 2015;**11**(5):298–307. <https://doi.org/10.1038/nrendo.2015.30>.
- Guha M, Bankura B, Ghosh S, Pattanayak AK, Ghosh S, Pal DK, Puri A, Kundu AK, Das M. Polymorphisms in CaSR and CLDN14 genes

- associated with increased risk of kidney stone disease in patients from the eastern part of India. *PLoS One* 2015;**10**(6):e0130790. <https://doi.org/10.1371/journal.pone.0130790>.
- Hannan FM, Walls GV, Babinsky VN, Nesbit MA, Kallay E, Hough TA, Fraser WD, Cox RD, Hu J, Spiegel AM, et al. The calcilytic agent NPS 2143 rectifies hypocalcemia in a mouse model with an activating calcium-sensing receptor (CaSR) mutation: relevance to autosomal dominant hypocalcemia type 1 (ADH1). *Endocrinology* 2015;**156**(9):3114–3121. <https://doi.org/10.1210/en.2015-1269>.
- He Y-H, He Y, Liao X-L, Niu Y-C, Wang G, Zhao C, Wang L, Tian M-J, Li Y, Sun C-H. The calcium-sensing receptor promotes adipocyte differentiation and adipogenesis through PPAR γ pathway. *Mol Cell Biochem*. 2012;**361**(1-2):321–328. <https://doi.org/10.1007/s11010-011-1118-5>.
- He Y-H, Song Y, Liao X-L, Wang L, Li G, Alima LY, Sun C-H. The calcium-sensing receptor affects fat accumulation via effects on antilipolytic pathways in adipose tissue of rats fed low-calcium diets. *J Nutr*. 2011;**141**(11):1938–1946. <https://doi.org/10.3945/jn.111.141762>.
- Heaney RP, Davies KM, Barger-Lux MJ. Calcium and weight: clinical studies. *J Am Coll Nutr*. 2002;**21**(2):152S–155S. <https://doi.org/10.1080/07315724.2002.10719213>.
- Ho C, Conner DA, Pollak MR, Ladd DJ, Kifor O, Warren HB, Brown EM, Seidman JG, Seidman CE. A mouse model of human familial hypocalciuric hypercalcemia and neonatal severe hyperparathyroidism. *Nat Genet*. 1995;**11**(4):389–394. <https://doi.org/10.1038/ng1295-389>.
- Hough TA, Bogani D, Cheeseman MT, Favor J, Nesbit MA, Thakker RV, Lyon MF. Activating calcium-sensing receptor mutation in the mouse is associated with cataracts and ectopic calcification. *Proc Natl Acad Sci U S A*. 2004;**101**(37):13566–13571. <https://doi.org/10.1073/pnas.0405516101>.
- Kamberov YG, Wang S, Tan J, Gerbault P, Wark A, Tan L, Yang Y, Li S, Tang K, Chen H, et al. Modeling recent human evolution in mice by expression of a selected EDAR variant. *Cell* 2013;**152**(4):791–702. <https://doi.org/10.1016/j.cell.2013.01.016>.
- Kanai M, Akiyama M, Takahashi A, Matoba N, Momozawa Y, Ikeda M, Iwata N, Ikegawa S, Hirata M, Matsuda K, et al. Genetic analysis of quantitative traits in the Japanese population links cell types to complex human diseases. *Nat Genet*. 2018;**50**(3):390–400. <https://doi.org/10.1038/s41588-018-0047-6>.
- Kapur K, Johnson T, Beckmann ND, Sehmi J, Tanaka T, Kutalik Z, Styrkarsdottir U, Zhang W, Marek D, Gudbjartsson DF, et al. Genome-wide meta-analysis for serum calcium identifies significantly associated SNPs near the calcium-sensing receptor (CASR) gene. *PLoS Genet*. 2010;**6**(7):e1001035. <https://doi.org/10.1371/journal.pgen.1001035>.
- Keane TM, Goodstadt L, Danecek P, White MA, Wong K, Yalcin B, Heger A, Agam A, Slater G, Goodson M, et al. Mouse genomic variation and its effect on phenotypes and gene regulation. *Nature* 2011;**477**(7364):289–294. <https://doi.org/10.1038/nature10413>.
- Kircher M, Witten DM, Jain P, O’Roak BJ, Cooper GM, Shendure J. A general framework for estimating the relative pathogenicity of human genetic variants. *Nat Genet*. 2014;**46**(3):310–315. <https://doi.org/10.1038/ng.2892>.
- Kristiansen MNB, Veidal SS, Rigbolt KTG, Tølbøl KS, Roth JD, Jelsing J, Vrang N, Feigh M. Obese diet-induced mouse models of non-alcoholic steatohepatitis-tracking disease by liver biopsy. *World J Hepatol*. 2016;**8**(16):673. <https://doi.org/10.4254/wjh.v8.i16.673>.
- Lassek WD, Gaulin SJ. Menarche is related to fat distribution. *Am J Phys Anthropol*. 2007;**133**(4):1147–1151. <https://doi.org/10.1002/ajpa.20644>.
- Li P, Fan C, Lu Y, Qi K. Effects of calcium supplementation on body weight: a meta-analysis. *Am J Clin Nutr*. 2016;**104**(5):1263–1273. <https://doi.org/10.3945/ajcn.116.136242>.
- Migliano AB, Romero IG, Metspalu M, Leavesley M, Pagani L, Antao T, Huang D-W, Sherman BT, Siddle K, Scholes C, et al. Evolution of the pygmy phenotype: evidence of positive selection from genome-wide scans in African, Asian, and Melanesian pygmies. *Hum Biol*. 2013;**85**(1-3):251–284. <https://doi.org/10.1353/hub.2013.a530634>.
- Migliano AB, Vinicius L, Lahr MM. Life history trade-offs explain the evolution of human pygmies. *Proc Natl Acad Sci U S A*. 2007;**104**(51):20216–20219. <https://doi.org/10.1073/pnas.0708024105>.
- Miranda VPN, de Faria FR, de Faria ER, Priore SE. Somatic maturation and body composition in female healthy adolescents with or without adjustment for body fat. *Rev Paul Pediatr*. 2014;**32**(1):78–84. <https://doi.org/10.1590/S0103-05822014000100013>.
- Mondal M, Casals F, Xu T, Dall’Olio GM, Pybus M, Netea MG, Comas D, Laayouni H, Li Q, Majumder PP, et al. Genomic analysis of Andamanese provides insights into ancient human migration into Asia and adaptation. *Nat Genet*. 2016;**48**(9):1066–1070. <https://doi.org/10.1038/ng.3621>.
- Nielsen TS, Jessen N, Jørgensen JOL, Møller N, Lund S. Dissecting adipose tissue lipolysis: molecular regulation and implications for metabolic disease. *J Mol Endocrinol*. 2014;**52**(3):R199–R222. <https://doi.org/10.1530/JME-13-0277>.
- Ohsu T, Amino Y, Nagasaki H, Yamanaka T, Takeshita S, Hatanaka T, Maruyama Y, Miyamura N, Eto Y. Involvement of the calcium-sensing receptor in human taste perception. *J Biol Chem*. 2010;**285**(2):1016–1022. <https://doi.org/10.1074/jbc.M109.029165>.
- Parlee SD, Lentz SI, Mori H, MacDougald OA. Quantifying size and number of adipocytes in adipose tissue. *Methods Enzymol*. 2014;**537**:93–122. <https://doi.org/10.1016/B978-0-12-411619-1.00006-9>.
- Perry GH, Dominy NJ. Evolution of the human pygmy phenotype. *Trends Ecol Evol*. 2009;**24**(4):218–225. <https://doi.org/10.1016/j.tree.2008.11.008>.
- Philip P, Matsumura H, Bulbeck D, editors. *New perspectives in Southeast Asian and Pacific prehistory*. Acton: ANU Press; 2017. <http://doi.org/10.22459/TA45.03.2017>.
- Pybus M, Dall’Olio GM, Luisi P, Uzkudun M, Carreño-Torres A, Pavlidis P, Laayouni H, Bertranpetit J, Engelken J. 1000 Genomes Selection Browser 1.0: a genome browser dedicated to signatures of natural selection in modern humans. *Nucleic Acids Res*. 2014;**42**(D1):D903–D909. <https://doi.org/10.1093/nar/gkt1188>.
- Ranieri M, Tamma G, Di Mise A, Vezzoli G, Soldati L, Svelto M, Valenti G. Excessive signal transduction of gain-of-function variants of the calcium-sensing receptor (CaSR) are associated with increased ER to cytosol calcium gradient. *PLoS One* 2013;**8**(11):e79113. <https://doi.org/10.1371/journal.pone.0079113>.
- Reyes M, Rothe HM, Mattar P, Shapiro WB, Cifuentes M. Antilipolytic effect of calcimimetics depends on the allelic variant of calcium-sensing receptor gene polymorphism rs1042636 (Arg990Gly). *Eur J Hum Genet*. 2012;**20**(4):480–482. <https://doi.org/10.1038/ejhg.2011.221>.
- Riccardi D, Brennan SC, Chang W. The extracellular calcium-sensing receptor, CaSR, in fetal development. *Best Pract Res Clin Endocrinol Metab*. 2013;**27**(3):443–453. <https://doi.org/10.1016/j.beem.2013.02.010>.
- Richardson CD, Ray GJ, DeWitt MA, Curie GL, Corn JE. Enhancing homology-directed genome editing by catalytically active and inactive CRISPR-Cas9 using asymmetric donor DNA. *Nat Biotechnol*. 2016;**34**(3):339–344. <https://doi.org/10.1038/nbt.3481>.
- Rocha C, Villalobos E, Fuentes C, Villarroel P, Reyes M, Díaz X, Mattar P, Cifuentes M. Preadipocyte proliferation is elevated by calcium sensing receptor activation. *Mol Cell Endocrinol*. 2015;**412**:251–256. <https://doi.org/10.1016/j.mce.2015.05.011>.
- Ronen R, Udpa N, Halperin E, Bafna V. Learning natural selection from the site frequency spectrum. *Genetics* 2013;**195**(1):181–193. <https://doi.org/10.1534/genetics.113.152587>.
- Rosenblum JL, Castro VM, Moore CE, Kaplan LM. Calcium and vitamin D supplementation is associated with decreased abdominal visceral adipose tissue in overweight and obese adults. *Am J Clin Nutr*. 2012;**95**(1):101–108. <https://doi.org/10.3945/ajcn.111.019489>.

- Sabeti PC, Varilly P, Fry B, Lohmueller J, Hostetter E, Cotsapas C, Xie X, Byrne EH, McCarroll SA, Gaudet R, et al. Genome-wide detection and characterization of positive selection in human populations. *Nature* 2007;**449**(7164):913–918. <https://doi.org/10.1038/nature06250>.
- Santa Maria C, Cheng Z, Li A, Wang J, Shoback D, Tu CL, Chang W. Interplay between CaSR and PTH1R signaling in skeletal development and osteoanabolism. *Semin Cell Dev Biol*. 2016;**49**:11–23. <https://doi.org/10.1016/j.semcdb.2015.12.004>.
- Scholes C, Siddle K, Ducourneau A, Crivellaro F, Järve M, Roots S, Bellatti M, Tabbada K, Mormina M, Reidla M, et al. Genetic diversity and evidence for population admixture in Batak Negritos from Palawan. *Am J Phys Anthropol*. 2011;**146**(1):62–72. <https://doi.org/10.1002/ajpa.21544>.
- Schreiweis C, Bornschein U, Burguière E, Kerimoglu C, Schreiter S, Dannemann M, Goyal S, Rea E, French CA, Puliyadi R, et al. Humanized Foxp2 accelerates learning by enhancing transitions from declarative to procedural performance. *Proc Natl Acad Sci U S A*. 2014;**111**(39):14253–14258. <https://doi.org/10.1073/pnas.1414542111>.
- Scillitani A, Guarnieri V, De Geronimo S, Muscarella LA, Battista C, D'Agruma L, Bertoldo F, Florio C, Minisola S, Hendy GN, et al. Blood ionized calcium is associated with clustered polymorphisms in the carboxyl-terminal tail of the calcium-sensing receptor. *J Clin Endocrinol and Metab*. 2004;**89**(11):5634–5638. <https://doi.org/10.1210/jc.2004-0129>.
- Siervogel RM, Demerath EW, Schubert C, Remsburg KE, Chumlea WC, Sun S, Czerwinski SA, Towne B. Puberty and body composition. *Horm Res Paediatr*. 2003;**60**(Suppl. 1):36–45. <https://doi.org/10.1159/000071224>.
- Spalding KL, Arner E, Westermark PO, Bernard S, Buchholz BA, Bergmann O, Blomqvist L, Hoffstedt J, Näslund E, Britton T, et al. 2008. Dynamics of fat cell turnover in humans. *Nature* **453**(7196):783–787. <https://doi.org/10.1038/nature06902>.
- Speidel L, Forest M, Shi S, Myers SR. A method for genome-wide genealogy estimation for thousands of samples. *Nat Genet*. 2019;**51**(9):1321–1329. <https://doi.org/10.1038/s41588-019-0484-x>.
- Stern AJ, Wilton PR, Nielsen R. An approximate full-likelihood method for inferring selection and allele frequency trajectories from DNA sequence data. *PLoS Genet*. 2019;**15**(9):e1008384. <https://doi.org/10.1371/journal.pgen.1008384>.
- Stock JT, Migliano AB. Stature, mortality, and life history among indigenous populations of the Andaman Islands, 1871–1986. *Curr Anthropol*. 2009;**50**(5):713–725. <https://doi.org/10.1086/605429>.
- Sun C, Wang L, Yan J, Liu S. Calcium ameliorates obesity induced by high-fat diet and its potential correlation with p38 MAPK pathway. *Mol Biol Rep*. 2012;**39**(2):1755–1763. <https://doi.org/10.1007/s11033-011-0916-x>.
- Tajima F. Statistical method for testing the neutral mutation hypothesis by DNA polymorphism. *Genetics* 1989;**123**(3):585–595. <https://doi.org/10.1093/genetics/123.3.585>.
- Thakker RV, Richard Bringham F, Jüppner H. Chapter 61 - Regulation of calcium homeostasis and genetic disorders that affect calcium metabolism. In: Jameson JL, De Groot LJ, de Kretser DM, Giudice LC, Grossman AB, Melmed S, Potts JT, Weir GC, editors. *Endocrinology: adult and pediatric*. 7th ed. Philadelphia (PA): Elsevier Saunders; 2016. p. 1063–1089.e10.
- Toka HR, Al-Romaih K, Koshy JM, DiBartolo S, Kos CH, Quinn SJ, Curhan GC, Mount DB, Brown EM, Pollak MR. Deficiency of the calcium-sensing receptor in the kidney causes parathyroid hormone-independent hypocalciuria. *J Am Soc Nephrol*. 2012;**23**(11):1879–1890. <https://doi.org/10.1681/ASN.2012030323>.
- Turksen K, Troy TC. Overexpression of the calcium sensing receptor accelerates epidermal differentiation and permeability barrier formation in vivo. *Mech Dev*. 2003;**120**(6):733–744. [https://doi.org/10.1016/S0925-4773\(03\)00045-5](https://doi.org/10.1016/S0925-4773(03)00045-5).
- Venkateswar S. *Development and ethnocide: colonial practices in the Andaman islands* (Christian E, Sille S, editors.). Copenhagen: IWGIA; 2004.
- Verdu P, Austerlitz F, Estoup A, Vitalis R, Georges M, Théry S, Froment A, Le Bomin S, Gessain A, Hombert JM, et al. Origins and genetic diversity of Pygmy. *Curr Biol*. 2009;**19**(4):312–318. <https://doi.org/10.1016/j.cub.2008.12.049>.
- Vergheze PB, Arrese EL, Soulagès JL. Stimulation of lipolysis enhances the rate of cholesterol efflux to HDL in adipocytes. *Mol Cell Biochem*. 2007;**302**(1-2):241–248. <https://doi.org/10.1007/s11010-007-9447-0>.
- Vezzoli G, Terranegra A, Arcidiacono T, Biasion R, Coviello D, Syren ML, Paloschi V, Giannini S, Mignogna G, Rubinacci A, et al. R990g polymorphism of calcium-sensing receptor does produce a gain-of-function and predispose to primary hypercalciuria. *Kidney Int*. 2007;**71**(11):1155–1162. <https://doi.org/10.1038/sj.ki.5002156>.
- Villarreal P, Reyes M, Fuentes C, Segovia MP, Tobar N, Villalobos E, Martínez J, Hugo E, Ben-Jonathan N, Cifuentes M. Adipogenic effect of calcium sensing receptor activation. *Mol Cell Biochem*. 2013;**384**(1-2):139–145. <https://doi.org/10.1007/s11010-013-1791-7>.
- Walker R, Gurven M, Hill K, Migliano A, Chagnon N, De Souza R, Djurovic G, Hames R, Hurtado AM, Kaplan H, et al. Growth rates and life histories in twenty-two small-scale societies. *Am J Hum Biol*. 2006;**18**(3):295–311. <https://doi.org/10.1002/ajhb.20510>.
- Walsh S, Izquierdo-Serra M, Acosta S, Edo A, Lloret M, Moret R, Bosch E, Oliva B, Bertranpetit J, Fernández-Fernández JM. Adaptive selection drives TRPP3 loss-of-function in an Ethiopian population. *Sci Rep*. 2020;**10**(1):20999. <https://doi.org/10.1038/s41598-020-78081-z>.
- Wang Y, Bikle DD, Chang W. Autocrine and paracrine actions of IGF-I signaling in skeletal development. *Bone Res*. 2013;**1**(3):249–259. <https://doi.org/10.4248/BR201303003>.
- Wang K, Li M, Hakonarson H. ANNOVAR: functional annotation of genetic variants from high-throughput sequencing data. *Nucleic Acids Res*. 2010;**38**(16):e164. <https://doi.org/10.1093/nar/gkq603>.
- Xu J, Kulkarni SR, Li L, Slitt AL. UDP-glucuronosyltransferase expression in mouse liver is increased in obesity- and fasting-induced steatosis. *Drug Metab Dispos*. 2012;**40**(2):259–266. <https://doi.org/10.1124/dmd.111.039925>.
- Zemel MB. Regulation of adiposity and obesity risk by dietary calcium: mechanisms and implications. *J Am Coll Nutr*. 2002;**21**(2):146S–151S. <https://doi.org/10.1080/07315724.2002.10719212>.
- Zhang F, Ye J, Meng Y, Ai W, Su H, Zheng J, Liu F, Zhu X, Wang L, Gao P, et al. Calcium supplementation enhanced adipogenesis and improved glucose homeostasis through activation of Camkii and PI3K/Akt signaling pathway in porcine bone marrow mesenchymal stem cells (pBMSCs) and mice fed high fat diet (HFD). *Cell Physiol Biochem*. 2018;**51**(1):154–172. <https://doi.org/10.1159/000495171>.
- Zhang F, Ye J, Zhu X, Wang L, Gao P, Shu G, Jiang Q, Wang S. Anti-obesity effects of dietary calcium: the evidence and possible mechanisms. *Int J Mol Sci*. 2019;**20**(12):3072. <https://doi.org/10.3390/ijms20123072>.